PAPER

Synthesis, characterization and computational studies of copper(II) terpyridine-based metal–organic frameworks for the removal of emerging herbicide contaminant from aqueous solution

Adedibu C. Tella, [ID] [a] Sunday J. Olatunji,[ab] Solomon O. Oloyede,[b] Allen T. Gordon,[c] Adeniyi S. Ogunlaja [ID] [c] and Peter A. Ajibade [ID] *[b]

Copper(II) metal–organic frameworks (MOFs) of 4,4',4''-tri-*tert*-butyl-2,2':6',2''-terpyridine(N_3ttb) formulated as [Cu(btc)(N_3ttb)]·(DMF)$_2$ **1** and [Cu(N_3ttb)(H$_2$O)$_2$] **2** (DMF = dimethylformamide) were synthesized and characterized by elemental analyses, and spectroscopic techniques, and compound **1** was further characterized by single crystal X-ray crystallography. The molecular structure of compound **1** revealed a five-coordinate geometry with three meridional nitrogen atoms of 4,4',4''-tri-*tert*-butyl-2,2':6',2''-terpyridine and two oxygen atoms of 1,3,5-benzenetricarboxylic acid to form a square pyramidal geometry. Compound **2** was functionalized with 1,2-ethanedithiol (TH) to prepared [Cu(N_3ttb)(H$_2$O)$_2$]–TH (compound **3**). The copper(II) metal–organic frameworks (MOFs) were used as adsorbents for the removal of 2,4-dichlorophenoxyacetic acid. The adsorption processes followed pseudo-second-order kinetics, and the adsorption equilibrium data best fit the Langmuir isotherm, with R^2 values of 0.981, 0.991, and 0.991 for **1**, **2** & **3** respectively. The quantity of 2,4-dichlorophenoxyacetic acid removed was 588.24, 333.33 and 833.33 mg g^{-1} over **1**, **2** & **3** respectively. The results indicate that the functionalized compound **3** has a higher adsorption capacity than **1** & **2** which could be ascribed to electrostatic interactions between the thiol groups of 1,2-ethanedithiol and the carboxylic acid group of 2,4-dichlorophenoxyacetic acid. Computational studies revealed that **3** outperforms **1** & **2** in herbicide adsorption, this can be adjudged to its ultra-soft character ($\eta = 0.31$ eV, $S = 1.61$ eV^{-1}), high electrophilicity ($\omega = 74.56$ eV) which enables charge-transfer-driven binding with both favourable ΔG (-39.500 kcal mol^{-1}) and high experimental capacity (833.33 mg g^{-1}). FT-IR spectroscopic analysis of the MOFs post-adsorption revealed the presence of the herbicide. The study's findings indicated that the prepared MOFs are effective adsorbent for removal of 2,4-dichlorophenoxyacetic acid from wastewater.

1 Introduction

Water is essential for all living organisms, as global health and development depend on it. Unfortunately, water quality is declining due to contamination by various harmful substances, including agrochemicals, dyes, metals, pharmaceuticals and personal care products.[1–4] In agriculture and industry, agrochemicals' widespread production and use, particularly pesticides, lead to water contamination in both surface and groundwater. Furthermore, as living standards rise and global food demand increases, pesticide production and utilization continue to grow. Numerous studies have shown that agrochemicals are present in wastewater treatment plant effluents, rivers, lakes, and occasionally in groundwater.[1] The impact of discharging effluents from agrochemical industries has been extensively discussed in scientific literature. Contaminants can be removed in several ways such as absorption,[4–10] degradation (bio, photodegradation, oxidative & ultrasound),[11–13] electrochemical,[1,14] chlorination,[4,15,16] membrane nanofiltration,[4,17] ozonation[4,18] and precipitation.[4] Furthermore, various environmental remediation methods and their associated limitations have been discussed, highlighting the necessity for adsorptive techniques to remove these effluents. Consequently, developing efficient adsorptive materials for 2,4-dichlorophenoxyacetic acid removal is important in both environmental and analytical sciences.[1,3] However, addressing the removal of these emerging contaminants from our drinking water and aquatic systems remains a crucial concern for researchers worldwide. Among the different methods studied, adsorption stands out due to its favourable features, including

[a]Department of Chemistry, University of Ilorin, P.M.B.1515, Ilorin, Kwara State, Nigeria

[b]Discipline of Chemistry, School of Agriculture and Science, University of KwaZulu-Natal, Private Bag X01, Scottsville 3209, South Africa. E-mail: ajibadep@ukzn.ac.za

[c]Department of Chemistry, Nelson Mandela University, P. O. Box 77000, Gqeberha, South Africa

gentle operating conditions, minimal investment, low energy consumption, and no oxidants or reductants.[1,4]

Porous materials like activated alumina, activated carbons, amberlite, birnessite, clay, kaoline, MOFs, sawdust, silica gel and zeolites.,[1,4,19–25] which possess high surface areas, are potential adsorbents. This is because adsorption depends on the porosity or surface area and the functionality of the adsorbent. MOFs have proven to be effective adsorbents because they can adsorb various hazardous substances from aqueous and nonaqueous environments. This is due to their remarkable porosity, adjustable pore structure, and ease of functionalization without altering the framework's topology.[1,4,26] Functionalization has been employed to enhance the efficiency of MOFs by introducing additional functional groups, such as amines and thiols, to their surface.[27–33] Metal–organic frameworks can be readily modified covalently with amino or thiol groups due to the availability of unsaturated central metal ions. These chemical modifications allow for the introduction of specific functional groups into MOFs, paving the way for the design of a new generation of enhanced MOFs.[27,28,30]

Herein, we report the synthesis and characterization of MOFs prepared from copper(II), 4,4′,4″-tri-*tert*-butyl-2,2′:6′,2″-terpyridine and 1,3,5-benzenetricarboxylic acid formulated as $[Cu(btc)(N_3ttb)]\cdot2(DMF)$ **1**, $[Cu(N_3ttb)(H_2O)_2]$ **2** and it's thiol functionalization to prepared $[Cu(N_3ttb)(H_2O)_2]$–TH **3**. The potential of the three MOFs to remove 2,4-dichlorophenoxyacetic acid from water was evaluated.

2 Experimental section

2.1. Materials

All chemicals utilized were of analytical grade and purchased from Sigma Aldrich. The research chemicals are 4,4′,4″-tri-*tert*-butyl-2,2′:6′,2″-terpyridine, 1,3,5-benzene tricarboxylic acid, copper(II) acetate dihydrate, dimethylformamide, ethanol, methanol, and water.

2.2. Synthesis of $[Cu(btc)(N_3ttb)]\cdot2(DMF)$ 1

1,3,5-Benzenetricarboxylic acid (H$_3$btc, 0.0160 g, 0.076 mmol), 4,4′,4″-tri-*tert*-butyl-2,2′:6′,2″-terpyridine (N$_3$ttb, 0.0305 g, 0.076 mmol) and copper(II) acetate monohydrate (Cu(CH$_3$COO)$_2$·H$_2$O, 0.0150 g, 0.076 mmol) were accurately weighed and dissolved in 15 mL of dimethylformamide/ethanol/methanol/water (1 : 1 : 1 : 1). The resulting solution was sonicated at 65 °C for 60 minutes then transferred to a glass vial and kept in the oven for five days at 65 °C. After 5 days, a translucent blue solution was obtained, which was left to slowly evaporate at room temperature. Green block crystals, suitable for single crystal X-ray diffraction, formed after 56 days. The green crystals formed were separated by filtration and washed with a mixture of dimethylformamide, ethanol, methanol and water in a ratio of 1 : 1 : 1 : 1 and dried at room temperature (Scheme S1 in the SI).

2.3. Synthesis of $[Cu(N_3ttb)(H_2O)_2]$ 2

20 mL ethanoic solution (ethanol/water in ratio 1 : 1) of 4,4′,4″-tri-*tert*-butyl-2,2′:6′,2″-terpyridine (N$_3$ttb, 0.2007 g, 0.5 mmol)

was gradually added to 10 mL aqueous solution of copper(II) acetate monohydrate (Cu(CH$_3$COO)$_2$·H$_2$O, 0.0999 g, 0.5 mmol) over a five minutes duration with continuous stirring at 70 °C. A transparent blue solution was obtained and refluxed at 70 °C for 60 minutes. Subsequently, 10 mL of dimethylformamide was introduced into the solution, followed by reflux at 70 °C for 24 h. A blue residue was obtained and separated by filtration. Subsequently, it was washed with a mixture of dimethylformamide, ethanol, and water in a 1 : 1:3 ratio and dried at room temperature (Scheme S2 in the SI).

2.4. Functionalization of $[Cu(N_3ttb)(H_2O)_2]$ 2

0.300 g of $[Cu(N_3ttb)(H_2O)_2]$ was activated at 150 °C for 18 h and subsequently suspended in 10 mL of toluene. 1 mL of 1,2-ethanedithiol (TH) was introduced to the suspension and stirred at 110 °C for 12 h. Brown crystalline powder was formed which was recovered by filtration, washed with EtOH (12 mL × 4) and then dried for 24 h at RT in a vacuum. The percentage of sulphur in the modified MOF was quantified with energy-dispersive X-ray spectroscopy (Scheme S3 in the SI).

2.5. Physical measurements

The ligands' and synthesized MOFs' FT-IR spectra (4000–600 cm^{-1}) were obtained from Bruker Alpha II FT-IR with ATR accessory. The elemental composition of synthesized MOFs was checked on Thermo Scientific Flash 2000 elemental analyzer with a TCD detector. The mass spectra were obtained from the waters Micromass LCT premier TOF-MS using ESI techniques. Scanning electron microscopy (SEM) images were obtained from Philips (FEI) XL30 SEM. The amount of 2,4-dichlorophenoxyacetic acid removed was determined using Agilent 1290 Infinity II liquid chromatography coupled with a diode array detector.

2.6. Crystallographic data collection and structural analysis

Single crystals of $[Cu(btc)(N_3ttb)]_2\cdot(DMF)_2$ **1** were obtained by slow evaporation of the compound in a mixture of DMF/ethanol/methanol/water in a ratio of 1 : 1 : 1 : 1 at RT. Details of the crystal parameters, data collection and refinements are listed in Table 1. The single crystals data of **1** was collected on a Bruker APEX-II CCD diffractometer fitted with an Oxford Cryostems low-temperature instrument, running at $T = 100.07$ K. Using Olex2,[34] the structure was solved with the XT[35] structure solution program using Intrinsic Phasing and refined with the XL[36] refinement package using least squares minimization. Table 2 shows the list of selected bond lengths and angles.

2.7. Adsorption experiment

Adsorption of 2,4-dichlorophenoxyacetic acid on **1**, **2** and **3** was studied with an aqueous solution of 2,4-dichlorophenoxyacetic acid (molecular formula: $C_8H_6Cl_2O_3$, molecular weight: 221.04 g mol^{-1}, Merck, 98%). A stock solution of 2,4-dichlorophenoxyacetic acid (200 mg L^{-1}) was prepared by dissolving 20 mg of 2,4-dichlorophenoxyacetic acid in 100 mL of deionized water. The herbicide's lower concentrations (5–

Table 1 Crystal data and structure refinement of $[Cu(btc)(N_3ttb)]_2 \cdot (DMF)_2$ **1**

Compound	$[Cu(btc)(N_3ttb)]_2 \cdot (DMF)_2$ **1**
Empirical formula	$C_{42}H_{53}CuN_5O_8$
Formula weight	819.43
Temperature/K	103.33
Crystal system	Triclinic
Space group	$P\bar{1}$
a/Å	12.6758(4)
b/Å	13.0824(4)
c/Å	13.8908(4)
α/°	69.9640(10)
β/°	71.5870(10)
γ/°	73.668(2)
Volume/Å^3	2014.27(11)
Z	2
ρ_{calc}/g cm^{-3}	1.351
μ/mm^{-1}	1.249
$F(000)$	866.0
Crystal size/mm^3	0.375 × 0.24 × 0.21
Radiation	CuKα ($\lambda = 1.54178$)
2θ range for data collection/°	6.984 to 143.122
Index ranges	$-15 \leq h \leq 15, -16 \leq k \leq 15, -17 \leq l \leq 17$
Reflections collected	46 817
Independent reflections	7471 [$R_{int} = 0.0343$, $R_{sigma} = 0.0213$]
Data/restraints/parameters	7471/0/519
Goodness-of-fit on F^2	1.022
Final R indexes [$I \geq 2\sigma(I)$]	$R_1 = 0.0548$, w$R_2 = 0.1558$
Final R indexes [all data]	$R_1 = 0.0581$, w$R_2 = 0.1605$
Largest diff. peak/hole/e Å^{-3}	1.38/−0.57

Table 2 Some selected bond angles and bonds lengths of $[Cu(btc)(N_3ttb)]_2 \cdot (DMF)_2$

Selected bond angles (°)		Selected bond lengths (Å)	
N1–Cu1–O3	95.33(8)	N1–Cu1	2.058(2)
N2–Cu1–O3	99.08(9)	N2–Cu1	1.938(3)
N3–Cu1–O3	93.41(8)	N3–Cu1	2.043(2)
O1–Cu1–O3	89.20(8)	O1–Cu1	1.910(2)
N1–Cu1–O1	100.03(9)	O3–Cu1	2.177(2)
N2–Cu1–N3	79.21(9)		
N1–Cu1–N2	79.76(9)		
N3–Cu1–O1	99.98(9)		
N1–Cu1–N3	158.25(9)		
N2–Cu1–O1	171.71(9)		

30 mg L^{-1}) were prepared by successive dilution of the stock solution with deionized water. The concentrations of 2,4-dichlorophenoxyacetic acid were determined by measuring the solution absorbance with a PerkinElmer Lambda 35 UV-visible Absorption Spectrometer at 283 nm. The calibration curve was derived from the UV spectra of standard solutions (5–200 mg L^{-1}) at a pH of 3.5. Before 2,4-dichlorophenoxyacetic acid adsorption, the MOFs were activated by heating under a vacuum at 150 °C for 24 h and were kept in a desiccator. After activation, 5 mg of each of the adsorbents (**1**, **2** and **3**) were weighed and immersed into Erlenmeyer flasks containing 50 mL of aqueous 2,4-dichlorophenoxyacetic acid solutions (5 mg L^{-1} to 200 mg L^{-1}). The suspensions were shaken in an incubator shaker at a constant speed of 160 rpm at 25 °C for a fixed time (10 min to 12 h). After adsorption for the fixed time,

an aliquot (2 mL) of the solution was removed using a disposable syringe equipped and filtered using a 0.45 μm PTFE syringe filter. The filtrate's concentration was determined using a PerkinElmer Lambda 35 UV-visible Absorption Spectrometer. The amount of 2,4-dichlorophenoxyacetic acid adsorbed onto the MOFs was obtained using the expression:[1,4,37,38]

$$q_{eq} = \frac{(C_0 - C_{eq})V}{m}$$

where q_{eq} is the equilibrium adsorption capacity of 2,4-dichlorophenoxyacetic acid adsorbed on the unit mass of adsorbent (mg g^{-1}), C_0 and C_{eq} are the initial and equilibrium concentrations of 2,4-dichlorophenoxyacetic acid (mg L^{-1}), V is the volume of the solution of the adsorbate in liters (L), and m is the amount of adsorbent in grams (g), respectively. After filtration, the solid residue was washed twice with water, allowed to dry at room temperature and further characterized with FT-IR, SEM and BET. The effect of absorbent, pH, temperature and time on 2,4-dichlorophenoxyacetic acid adsorption over **1**, **2** and **3** were studied by adjusting the necessary parameters. The reusability of the absorbents (**1**, **2** and **3**) was determined by reusing **1**, **2** and **3** after simple purification by washing the MOFs with water, drying and reactivation.

3 Results and discussions

3.1. Synthesis

Compounds **1** and **2** were synthesized following the well-established procedure.[27,39] The self-assembly of $[Cu(btc)(N_3ttb)]_2 \cdot (DMF)_2$ in a DMF/ethanol/methanol/water ($1:1:1:1$)

mixture at room temperature resulted in the formation of a water-insoluble green dinuclear copper(II)-MOF crystals suitable for single crystals X-ray crystallography (Scheme S1). Compound **1** was only soluble in dimethyl sulfoxide (DMSO), and its insolubility in other typical organic solvents may be attributed to its polymeric characteristics. Compound **1** has been structurally characterized using a variety of analytical techniques, including CHN, FT-IR, MS and SC-XRD analysis.

SC-XRD analysis confirms that the asymmetric unit of the Cu-MOF contains one Cu(II) metal ion, one N_3ttb, one deprotonated $[btc]^{2-}$ and two DMF. The melting point, FT-IR spectra, elemental analysis and mass spectra data of the synthesized Cu-MOF unequivocally supported the formation of compound **1**, as confirmed by its X-ray crystal structure. $[Cu(N_3ttb)(H_2O)_2]$ **2** was only soluble in dimethylformamide (DMF) and was characterized by CHN, FT-IR and MS.
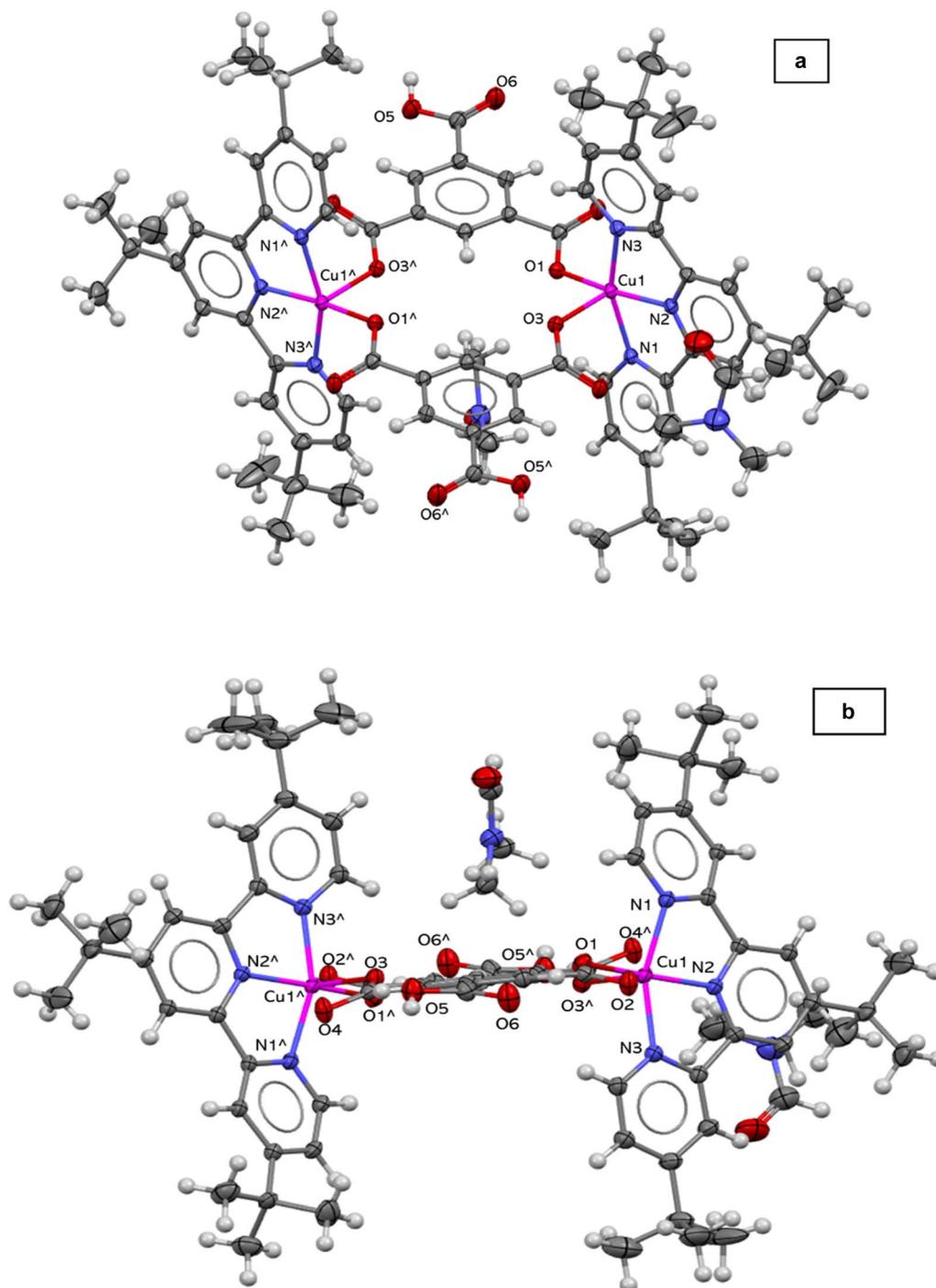
Fig. 1 Ortep diagram of $\{[C_{72}H_{78}Cu_2N_6O_{12}]\cdot(DMF)_2\}$ showing the two coordinated molecules of trimesic acid (a), the two coordinated terpyridine molecules (b) with non-hydrogens and carbon atoms numbering around the copper(II) ions.
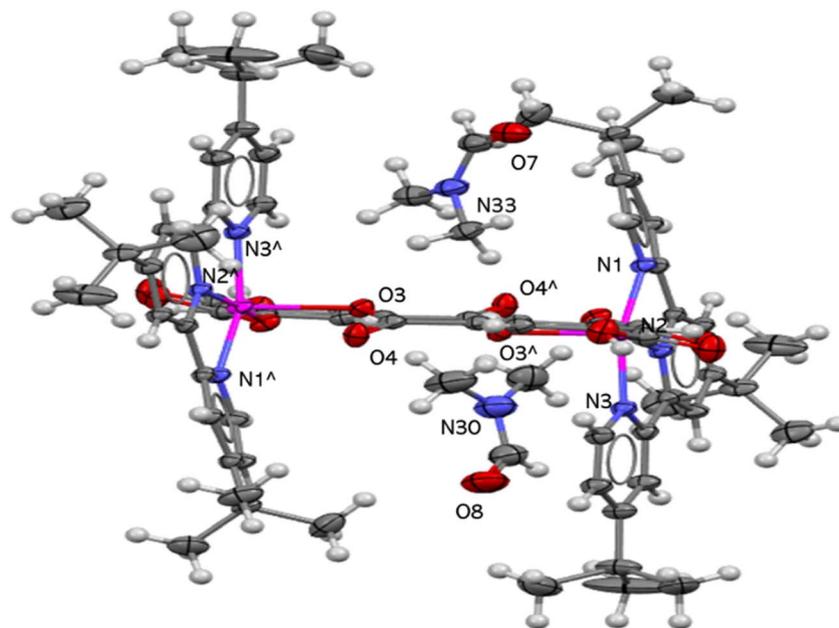
Fig. 2 Ortep diagram of {[$C_{72}H_{78}Cu_2N_6O_{12}$]·(DMF)$_2$} showing the two non-coordinated molecules of dimethylformamide with non-hydrogens and carbon atoms numbering around the copper(II) ions.

3.2. Molecular description of {[$C_{72}H_{78}Cu_2N_6O_{12}$](DMF)$_2$} (1)

The ORTEP representation revealing atoms numbering (without hydrogen, and carbon) of compound **1**, {[Cu(btc)(N$_3$ttb)]$_2$·(DMF)$_2$}, {[$C_{72}H_{78}Cu_2N_6O_{12}$](DMF)$_2$} showing the two coordinated benzene 1,3,5-tricarboxylic acid (H$_3$btc), and the two coordinated terpyridine molecules (N$_3$ttb) to the copper(II) ions are illustrated in Fig. 1(a) and (b) respectively. Fig. 2 displays the two molecules of dimethylformamide (DMF) acting as solvent of coordination. The packing diagram of compound **1**,

[Cu(btc)(N$_3$ttb)]$_2$·2(DMF), revealed one fitted molecule, and atoms fitted in the unit cell are presented in Fig. 3(a) and (b). Fig. 4(a) and (b) illustrates the Ortep diagram of compound **1**, [Cu(btc)(N$_3$ttb)]$_2$·(DMF)$_2$, showing intramolecular hydrogen bonding (A), and intermolecular hydrogen bonding (B) with non-hydrogen and carbons atoms numbering. Crystal data and structure refinement of [Cu(btc)(N$_3$ttb)]$_2$·(DMF)$_2$ is presented in Table 1, while some selected bond lengths and bonds angles are given in Table 2. Compound **1** crystallized in triclinic crystal system with a space group P1, primitive as the lattice type with
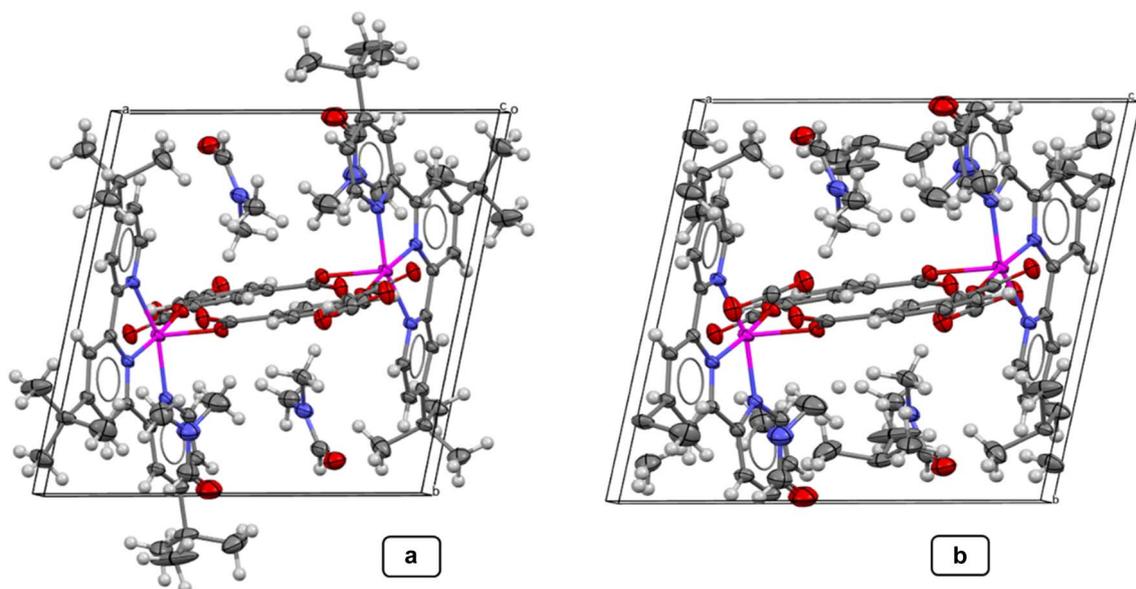

Fig. 3 Packing diagram of [Cu(btc)(N$_3$ttb)]$_2$·(DMF)$_2$ showing one fitted molecule in a unit cell (a), and atoms fitted in a unit cell (b).
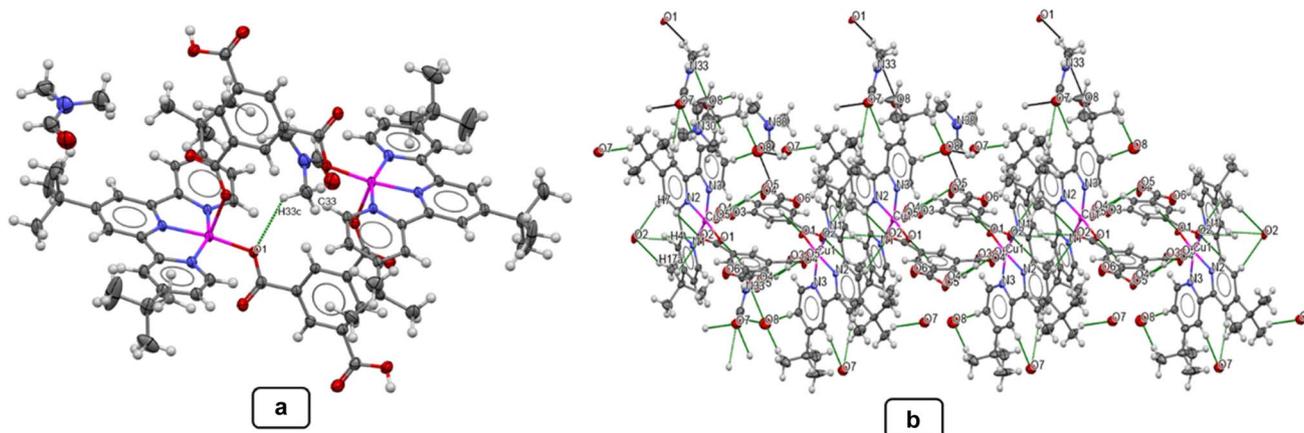
Fig. 4 Ortep diagram of $[Cu(btc)(N_3ttb)]_2 \cdot (DMF)_2$ showing intramolecular hydrogen bonding (a) and intermolecular hydrogen bonding (b) with non-hydrogen and carbon atoms numbering.

the cell length $a = 12.68(4)$ Å, $b = 13.08$ Å, $c = 13.89$ Å, the cell angles $\alpha = 69.96(10)°$, $\beta = 71.59(10)°$, and $\gamma = 73.61°$, and a cell volume 2014.27 Å³. Compound **1**, $[Cu(btc)(N_3ttb)]_2 \cdot (DMF)_2$, is a three-dimensional binuclear unit of copper(II) complex which is bridged by two molecules of benzene 1,3,5-tricarboxylic acid (H_3btc) to the two copper(II) ions through the hydroxyl oxygen of the anisobidentate-carboxylato group of the bridging ligand, and two tridentate molecules of terpyridine ((N_3ttb)) through three meridional nitrogen atoms coordinated to each copper(II) ion. The single crystal showed a distorted pentagonal coordination geometry around each copper(II) ion with the chromophore CuN_3O_2. Compound **1**, $[Cu(btc)(N_3ttb)]_2 \cdot (DMF)_2$, is a centrosymmetric dimer with a pentagonal chair like conformation at the centre of symmetry, like reported arrangement for copper(II) complex.[40]

The value of the geometry index or structural parameter for five coordinates geometry is given by Tau equation "$\tau = (\beta - \alpha)/60$" ($\beta$ = the first largest angle, and α = the second largest angle) which determined whether the five coordinate is square pyramidal (SP) or trigonal bipyramidal (TBP).[41] The value of Tau obtained for compound **1**, $[Cu(btc)(N_3ttb)]_2 \cdot (DMF)_2$, is

approximately 0.224 which is much closer to null (0) i.e. ($0.00 < \tau < 0.50$) than to unity (1) i.e. ($0.50 < \tau < 1.00$), submitting that the geometry around each of the copper(II) ions is a distorted square pyramidal with N_3ttb and a molecule of btc which occupy the equatorial plane and the second molecule of btc which occupy the axial plane of the geometry, with an inversion symmetry having the symmetry operation $-x, -y, -z$. Fig. 5 showed the polyhedral projection diagram of compound **1**, $[Cu(btc)(N_3ttb)]_2 \cdot (DMF)_2$ which confirmed the distortion of the square pyramidal geometry. The bonds lengths of N1–Cu1, N2–Cu1, N3–Cu1, O1–Cu1, and O3–Cu1 are 2.058(2) Å, 1.938(3) Å, 2.043(2) Å, 1.910(2) Å, and 2.177(2) Å respectively which revealed the longer length of O3–Cu1 compared to the remaining four bond lengths, and the discrepancy in bond lengths between N1–Cu1, N2–Cu1, N3–Cu1, O1–Cu1 confirmed further the distortion of the square pyramidal and anisobidentate character of the bridging ligand.[42] The bond lengths observed at the equatorial axes (N1–Cu1, N2–Cu1, N3–Cu1, O1–Cu1) which range between 1.900 Å to 2.060 Å, and the bond length at the axial axis (Cu –O3) are comparable to the bond length of Cu–N, Cu–O experienced in an ideal square pyramidal geometry ranging 1.900 Å to 2.100 Å, and 2.100 Å to 2.300 Å.[43] The values of adjacent angles at the basal plane of the distorted square pyramidal geometry N3–Cu1–O1 and N2–Cu–N1 are 99.98° and 79.76° respectively; N3–Cu1–N2, and N1–Cu1–O1 are 99.08° and 100.03°. This discrepancy experienced in the values of adjacent angles at the basal plane of the distorted square pyramidal compared to the equal adjacent angles at the basal plane of perfect square pyramidal confirmed further the distortion of the square pyramidal geometry.[44] The stability and the polymeric chain of compound **1**, $[Cu(btc)(N_3ttb)]_2 \cdot (DMF)_2$ is depicted through the intramolecular and intermolecular hydrogen bonding Fig. 4(a) and (b) respectively. The two non-coordinated dimethylformamide molecules further established the polymeric form of the compound through the intermolecular hydrogen bonding.[45] The intramolecular hydrogen bonding 'D–H···A' (where 'D' and 'A' stand for donor and acceptor atoms respectively) of the compound is observed through C_{33}–H_{33B}···
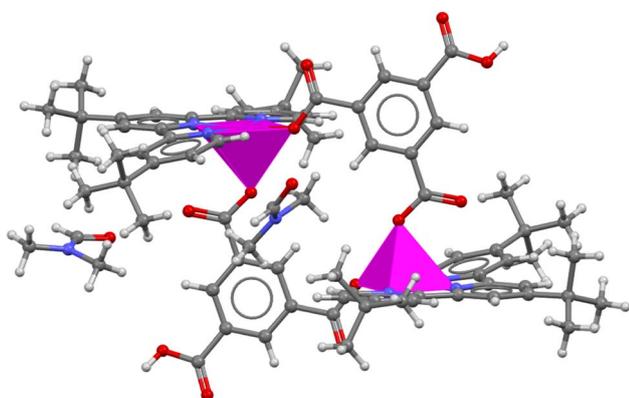

Fig. 5 Polyhedral diagram showing the geometry of $[Cu(btc)(N_3ttb)]_2 \cdot (DMF)_2$.

O_1 where the distance between the donor atom (C_{33}) and acceptor (O_1) is observed to be 3.270 Å, and the distance between the hydrogen (H_{33B}) and the acceptor (O_1) is observed to be 2.526 Å. This intramolecular hydrogen bonding stabilized the molecular conformation by locking the molecule in a specific shape, pre-organized the molecular geometry by orienting the molecule for favorable packing in the crystal lattice, and influence the crystal density.[46] Various intermolecular hydrogen bonding are also observed in the polymeric chain of the compound through C_{39}–$H_{39}\cdots O_5$ where the distance between the donor atom (C_{39}) and acceptor (O_5) is observed to be 3.189 Å, and the distance between the hydrogen (H_{39}) and the acceptor (O_5) is observed to be 2.404 Å; through C_{38}–$H_5\cdots O_4$ where the distance between the donor atom (C_{38}) and acceptor (O_4) is observed to be 2.732 Å, and the distance between the hydrogen (H_5) and the acceptor (O_4) is observed to be 1.715 Å; through C_{17}–$H_{17A}\cdots O_2$ where the distance between the donor atom (C_{17}) and acceptor (O_2) is observed to be 3.566 Å, and the distance between the hydrogen (H_{17A}) and the acceptor (O_2) is observed to be 2.663 Å; through C_4–$H_4\cdots O_2$ where the distance between the donor atom (C_4) and acceptor (O_2) is observed to be 3.066 Å, and the distance between the hydrogen (H_4) and the acceptor (O_2) is observed to be 2.435 Å; through C_7–$H_7\cdots O_2$ where the distance between the donor atom (C_7) and acceptor (O_2) is observed to be 3.366 Å, and the distance between the hydrogen (H_7) and the acceptor (O_2) is observed to be 2.574 Å.
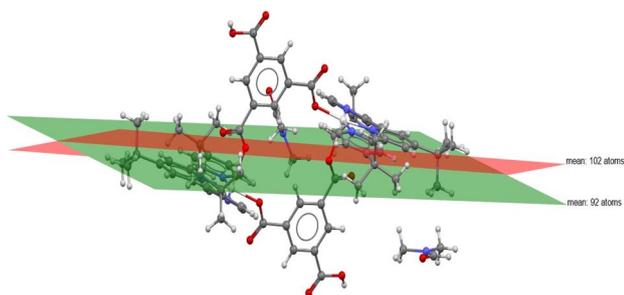
These intermolecular hydrogen bonding influenced the morphology of the compound, enhanced the melting and boiling point, facilitated network formation, and promoted the arrangement of molecules in the crystal lattice through a rigid structure.[47] The two planes which illustrated the inversion symmetry of the compound is depicted in Fig. 6, between btc molecules with mean of 102 atoms and through the ring of N_3ttb with a mean of 92 atoms.[48] The crystal compound was fictitiously packed at positions "*a*" and "*c*" to visualize the inclusion of solvent or small molecules inside the crystal lattice. Small molecules or solvent could be clearly trapped in the crystal pore (Fig. 7). The void space through contact surface (Fig. 7(a)) of the crystal was explored at a radius of 0.5 Å and an approximate grid spacing of 0.3 Å. Its volume, 326.45 Å^3, represents 16.3% of the unit cell volume. Additionally, the void space through solvent-accessible surface (Fig. 7(b)), which was probed at 0.5 Å with 0.3 Å grid spacing, had a volume of 69.40 Å^3, or signifies 3.4% of the unit cell volume. Fig. 8(a) and (b) further confirmed the polymeric chain of the compound through the '*a*-axis' and '*b*-axis'.

3.3. Infrared spectra studies of 1 and 2

Infrared spectra of compounds **1** and **2** were compared with those of the ligands (Fig. S1 and S2). Relevant IR bands in the Cu-MOFs are identified as ν(O–H), ν(C–H), ν(C=O), ν(C=C), ν(C–O), ν(C–N), ν(M–O) and ν(M–N). The Cu-MOFs spectra showed a significant shift in the ν(C–N) stretching frequency compared to the N_3ttb. The sharp strong absorption band of ν(C–N) observed at 1371 cm^{-1} in N_3ttb has shifted to 1386 cm^{-1} and 1379 cm^{-1} in **1** and **2** respectively. This shift indicates that pyridyl N-atoms are involved in the complexation. This binding approach aligns well with previous study.[27] The strong ν(C=O) and ν(C–O) absorption bands observed at 1720 cm^{-1} and 1276 cm^{-1} in the H_3btc have shifted to 1654 cm^{-1} and 1345 cm^{-1} in **1**, which is an indication that the carboxyl groups (COO$^-$) are involved in the complexation.[48] In addition, compound **1** spectrum showed a significant shift in the ν(O–H) stretching frequency compared to the H_3btc. The broad absorption band of ν(O–H) observed at 3084 cm^{-1} in H_2btc has shifted to 3447 cm^{-1} in **1**. The increase in the absorption band

Fig. 6 Diagram of [Cu(btc)(N_3ttb)]$_2$·(DMF)$_2$ showing the two planes between the trimesic molecule with mean of 102 atoms and through the ring of N_3ttb with a mean of 92 atoms.
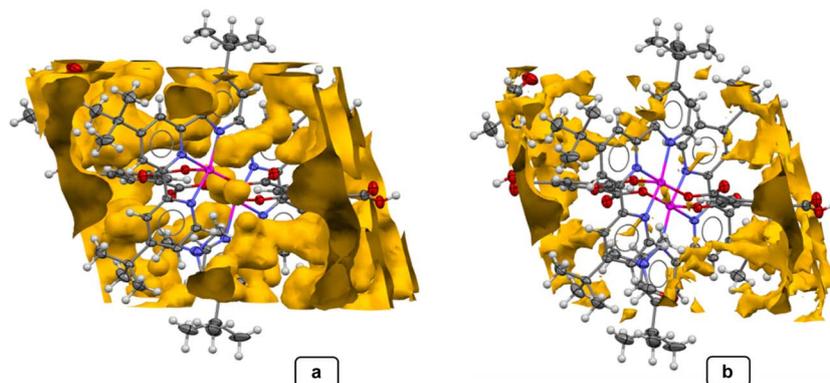

Fig. 7 Void space through contact surface (a) and through solvent accessible surface (b) of [Cu(btc)(N_3ttb)]$_2$·(DMF)$_2$.

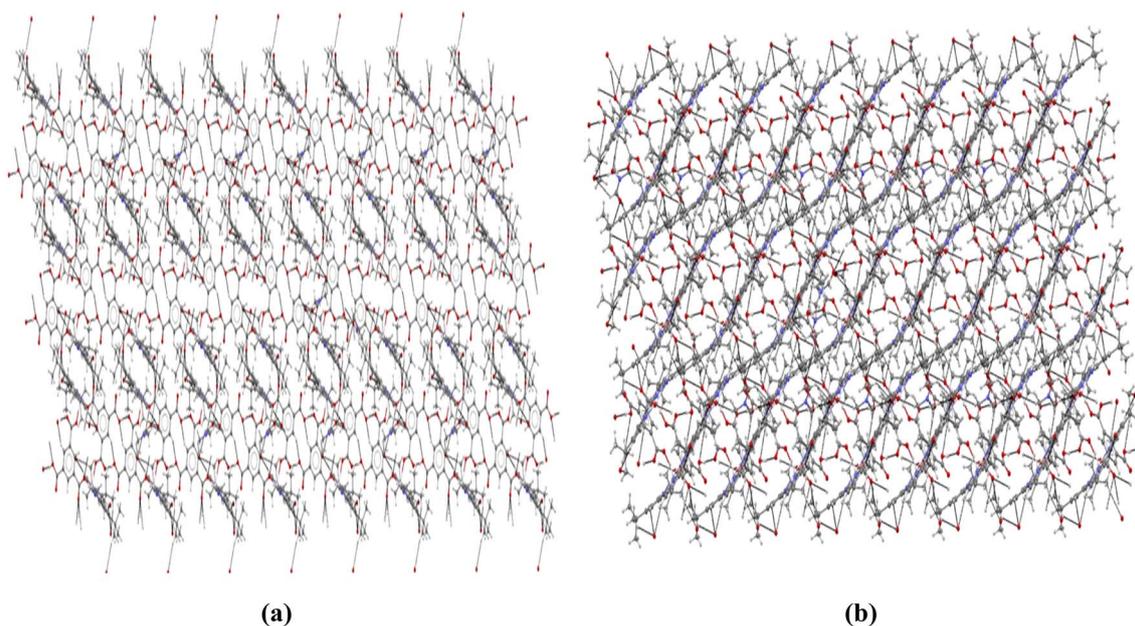**Fig. 8** Polymeric Chain representation of $[Cu(btc)(N_3ttb)]_2 \cdot (DMF)_2$ along a-axis (a), and along b-axis (b).

of uncoordinated –OH in H_3btc can be attributed to hydrogen bonding within the crystal lattice of the compound. This hydrogen bonding can alter the vibrational energy levels of the –OH group, leading to changes in the absorption band. The appearance of sharp absorption bands between 3115 cm^{-1} to 2850 cm^{-1} bands in the two MOFs could be attributed to aliphatic and aromatic ν(C–H) stretching vibrations.[27] The appearance of absorption bands between the 750 cm^{-1} and

600 cm^{-1} in the two synthesized Cu-MOFs provides information about the vibrational bands associated with ν(M–O) and ν(M–N) bonding.[27,49]

3.4. Mass spectra studies of 1 and 2

$[Cu(btc)(N_3ttb)] \cdot (DMF)_2$ (**1**) and $[Cu(N_3ttb)(H_2O)_2]$ (**2**) dissolved in dimethylsulfoxide without structural damage as seen on the mass spectra. The mass spectra of **1** and **2** were obtained and
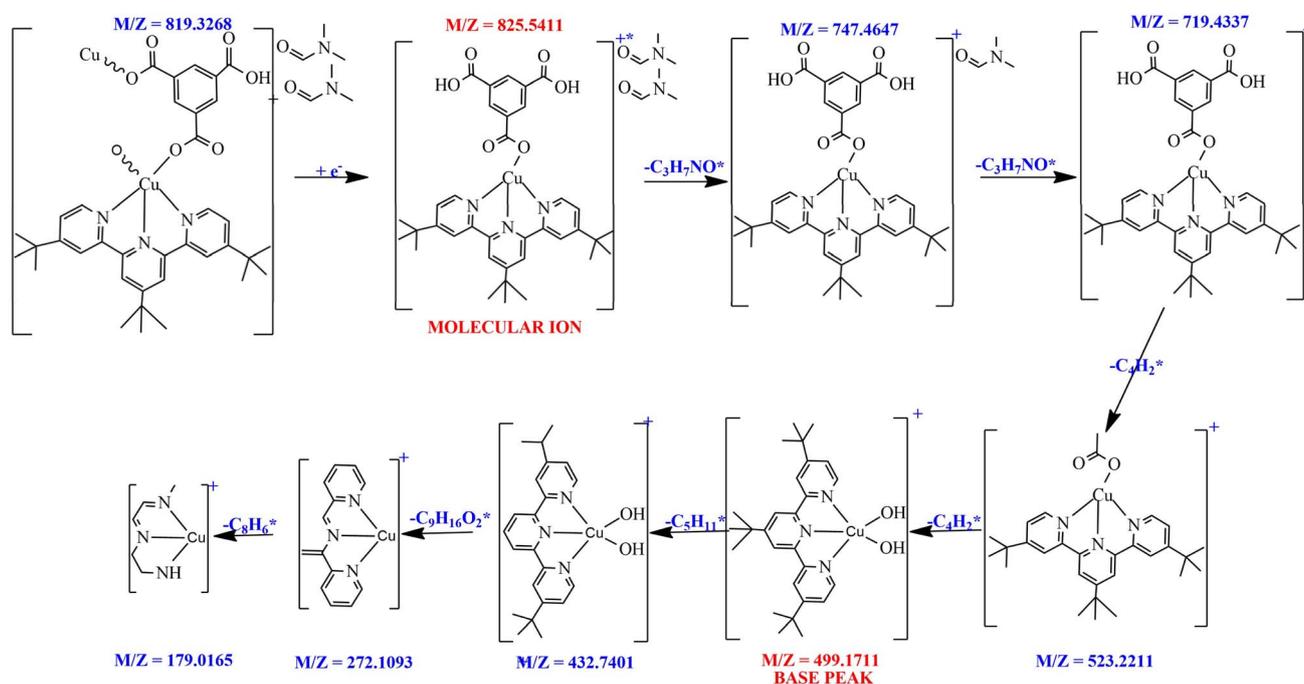

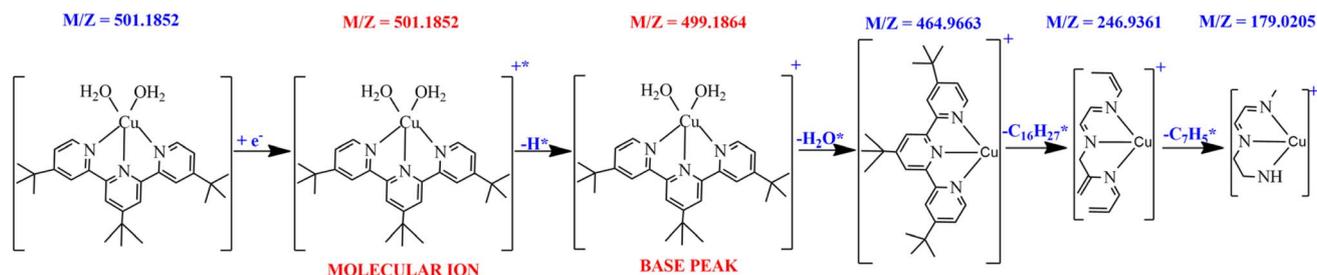**Fig. 9** Fragmentation mechanism of **1**.

Fig. 10 Fragmentation mechanism of **2**.

compared with those of the ligands (4,4′,4″-tri-*tert*-butyl-2,2′:6′,2″-terpyridine and 1,3,5-benzenetricarboxylic acid). The two Cu-MOFs mass spectra as depicted in Fig. S3 and S4, reveal that the molecular ion peaks are 825.54 *m/z* (calculated at 820.33 g mol^{-1}) and 501.19 *m/z* (calculated at 501.19 g mol^{-1}) for **1** and **2** respectively, which perfectly match with the empirical formula and the molecular weight determined from CHN analysis. Moreover, the fragmentation pattern depicted in Fig. 9 aligns with the peaks observed in the mass spectra and is confirmed with single crystal X-ray crystallography.

The mass spectra of **1** and **2** show similar fragmentation patterns and the same base peak due to their coordination with 4,4′,4″-tri-*tert*-butyl-2,2′:6′,2″-terpyridine (N_3ttb). After ionization, the molecular/parent ions $[C_{42}H_{54}CuN_5O_8]^{+*}$ and $[C_{27}H_{39}CuN_3O_2]^{+*}$ were formed by **1** and **2** respectively, as shown in Fig. 9 and 10. Following ionization of **1**, the DMF molecules solvent of crystallization were the first to be lost from the parent ions to produce $[C_{36}H_{40}CuN_3O_6]^+$. The appearance of the most intense peak (base peak) at 499.17 *m/z* in the spectra of the two Cu-MOFs is due to the formation of $[C_{27}H_{37}CuN_3O_2]^+$. The base peaks of these MOFs are similar to the base peak of the Cu-MOFs reported by Tella *et al.*, 2024.[27] After several fragmentations from the base peak ion, the smallest ion 179.02 *m/z* was formed due to the formation of $[C_5H_{10}CuN_3]^+$, which confirms the coordination of copper(II) ion with 4,4′,4″-tri-*tert*-butyl-2,2′:6′,2″-terpyridine through the three meridional nitrogen atoms. This binding approach aligns well with the research reported in the literature.[27,39–45]

3.5. Hirshfeld surface analysis

Hirshfeld Surface Analysis (HSA)[50–52] is a powerful technique for investigating intermolecular interactions within a crystal
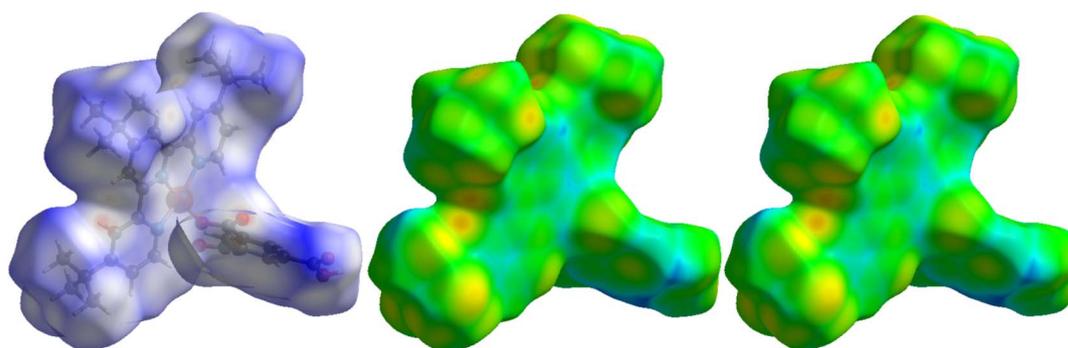

Fig. 11 3-D Hirshfeld surfaces mapped with (a) d_{norm}, (b) d_i and (c) d_e of **1**.
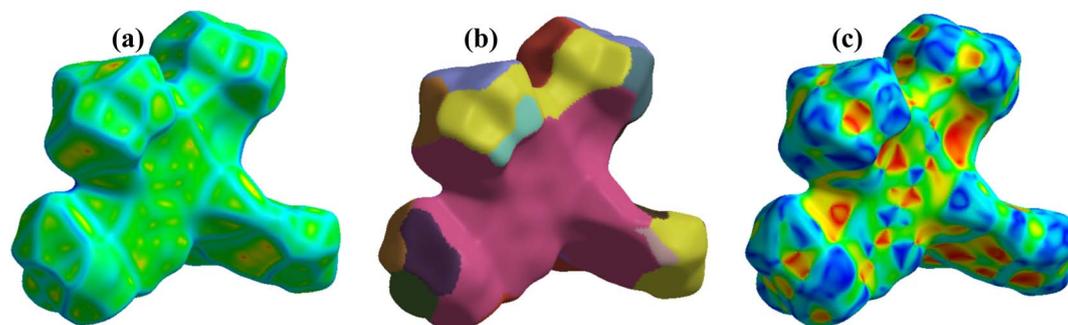
Fig. 12 3-D Hirshfeld surfaces mapped with (a) curvedness, (b) fragment patch and (c) shape index of **1**.
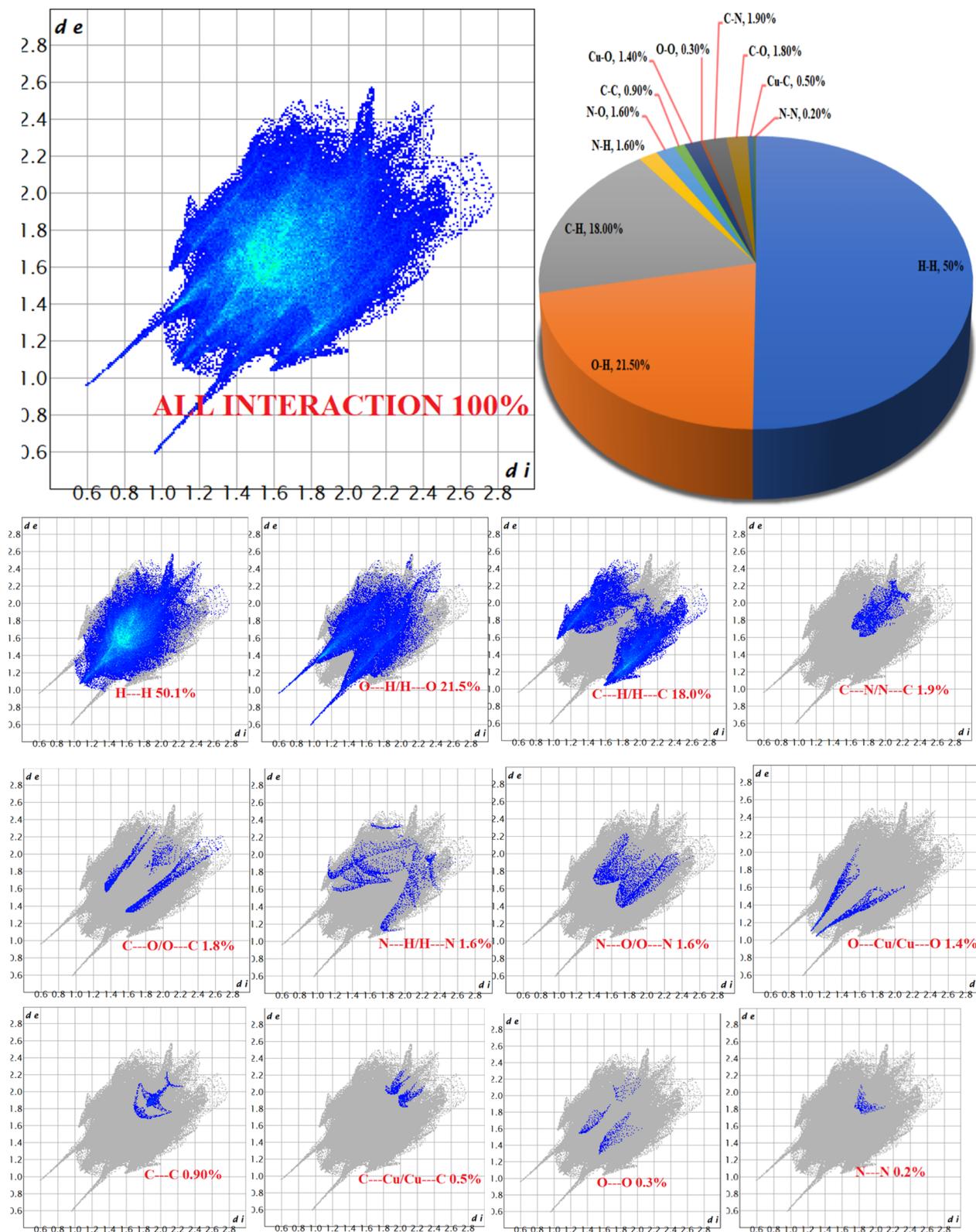
Fig. 13 2D fingerprint plots for **1** of different intermolecular interactions.

structure. This technique stands out for its capability to calculate and visually represent these interactions, resulting in distinct outcomes for each crystal structure. The analysis is performed by inputting the crystallographic information file (CIF) of the molecule under study into the Crystal Explorer 21.5 software.[53] Hirshfeld surfaces for compound **1** were generated

and mapped with d_e, d_i, and d_{norm}, shape index, curvedness, and two-dimensional fingerprint plots as shown in Fig. 11–13. The d_{norm} function is the ratio between the distance from the surface to the nearest nucleus internal to the surface (d_i) and the distance from the surface to the nearest nucleus external to the surface (d_e).[27,54] Fig. 11 depicts the Hirshfeld surface maps for d_{norm}, d_i and d_e of compound **1**. The d_{norm}, d_i and d_e were mapped over the ranges −0.8069 to 1.7898 Å, 0.6056 to 2.5995 Å & 0.6054 to 2.7884 Å respectively. The d_{norm} surface was drawn with blue, red, and white colours, where the blue colour region represents the distance of intermolecular interactions greater than van der Waals distance (d_{norm} = +ve), the red colour region represents the distance of intermolecular interactions lower than van der Waals distance (d_{norm} = −ve) while the white colour region represent the distance of intermolecular interactions equal to van der Waals distance (d_{norm} = 0).[27,55] The bright red spots on the crystal surface in the d_{norm} mapping indicate close contacts between neighbouring molecules. Specifically, there is close contact between the oxygen atom on 1,3,5-benzenetricarboxylic acid and the neighbouring central copper(ii) ion. The d_e and d_i surfaces indicate that the internal intermolecular interactions are stronger toward the tertiary –CH$_3$ group on 4,4′,4″-tri-tert-butyl-2,2′:6′,2″-terpyridine while the external intermolecular interactions are more around the Cu and O atoms.[27]

Fig. 12 depicts the Hirshfeld surface maps for curvedness, fragment patch and shape of the molecule compound **1**. The curvedness surface analysis was mapped over the range −4.0000 to 0.4000 Å for **1**. This surface is a measure of curvature in the total Hirshfeld map. As shown in Fig. 12a, the surface of compound **1** features numerous large green flat areas separated by blue edges, indicating high values of curvedness. These areas provide insights into interactions between neighbouring molecules (π⋯π stacking interactions).[27,39,56]

Fragment patch surfaces were mapped over the range from 0.0000 to 23.0000 Å for **1** as shown in Fig. 12(b). This mapping colour patch enables us to identify the closest neighbour coordination environment of molecule **1**.[57] Shape index was mapped over the range −1.0000 (concave) to 1.0000 (convex) Å for **1** as shown in Fig. 12(c). This surface demonstrates that the shape of the electron density surface encompasses the interactions between molecules. The shape index was drawn with blue, red, and green colours, where the blue-coloured region represents the concave areas, which indicates that the atoms of the π-stacked molecule above them while the red-coloured region represents convex areas, that indicates the ring atoms of the molecule within the surfaces.[57,58]

The 2D fingerprint plots for **1** as shown in Fig. 13 reveal there are twelve (12) intermolecular atomic interactions in the crystal structure. The intermolecular interactions through H⋯H, O⋯H and C⋯H were found to be dominant with 50.1%, 21.5% and 18.0% of all interactions respectively. The percentage of other intermolecular interactions are 1.9%, 1.8%, 1.6%, 1.6%, 1.4%, 0.9%, 0.5%, 0.3% and 0.2% for C⋯N, C⋯O, N⋯H, N⋯O, Cu⋯O C⋯C, Cu⋯C, O⋯O and N⋯N respectively.

Additionally, the form index surface shows that the arrangement of adjacent blue and red triangles around

compound **1** unit provides evidence for π–π stacking interactions between aromatic cycles, as illustrated in Fig. 11 and 12. The observed percentages of interactions contributing to **1** are depicted in Fig. 13. Notably, this quantitative analysis highlights that H⋯H interactions play a dominant role in the crystal structure. The findings from the Hirshfeld surface analysis align with those observed in the X-ray diffraction analysis.[27] The volume enclosed by the Hirshfeld surface is calculated to be 783.78 Å^3, with an area of 670.56 Å^2.

3.6. Thiol functionalization of 2

The thiol-functionalization of **2** through the coordination of 1,2-ethanedithiol (TH) to the unsaturated copper(ii) center of the dehydrated **1** framework was carried out as described in Section 2.4. After activation and modification, the Cu-MOF changes from blue to brown. **3** was air-stable and insoluble in water, methanol, isopropanol, ethyl acetate, ethanol, dimethyl sulfoxide, dichloromethane, chloroform, acetonitrile, and acetone. Apart from the colour change, the thiol-functionalization was confirmed by SEM, CHNS and FT-IR. The FT-IR, PXRD spectra as shown in Fig. S5 and S6 confirmed the addition of the thiol functional group into the MOFs framework network.[27–30] The PXRD of the as-synthesized and functionalized MOFs are the same which indicates that thiol-functionalization did not change the crystal lattice of compound **1**.[27–30] Fig. S5 shows the FTIR spectra of the 1,2-ethanedithiol, pristine, dehydrated and modified Cu-MOFs. After activation of **2**, there was no difference in the spectrum obtained. After the thiol functionalization of the Cu-MOFs through the coordination of 1,2-ethanedithiol (ET) to the unsaturated Cu(ii) ion, new band was observed at 2866 cm^{-1} for **3** which is a characteristic band of ν(S–H) vibrations. Although the peaks at 2866 cm^{-1} and 2907 cm^{-1} corresponding to ν(S–H) have shifted to larger values as observed when the molecule is coordinated to a Lewis acid center.[30] In addition to ν(S–H) vibrations, band was observed at 667 cm^{-1} in **3** which is a characteristic band of ν(C–S) vibrations. The findings unambiguously establish that 1,2-ethanedithiol molecules were effectively coordinated to the unsaturated central copper(ii) ion within the framework, rather than being adsorbed onto the external surface of the MOFs. This emphasizes the specific location of the coordination and distinguishes it from mere surface adsorption.[29] To investigate the chemical composition and surface morphology of the pristine and modified MOFs, the samples were characterized with SEM-EDX as shown in Fig. 14 and 15. Before the thiol-functionalization, **2** samples were cylindrical with large particles (Fig. 14) but after the thiol-functionalization, the sample was still cylindrical but with smaller particles (Fig. 9).[30]

Elemental analysis of **2** and **3** samples show that the compounds are made up of carbon, nitrogen, oxygen, sulphur and copper as depicted. Comparison of the CHNS result of the pristine and modified MOFs clearly shows the formation of [Cu(N$_3$ttb)(H$_2$O)$_2$]–ET **3**. After the functionalization of **2**, the percentage composition of sulphur (S) in **2** increased from 0.00% to 15.25% in **3**. This confirms the introduction of sulphur from 1,2-ethanedithiol (TH) into **2**.[30]
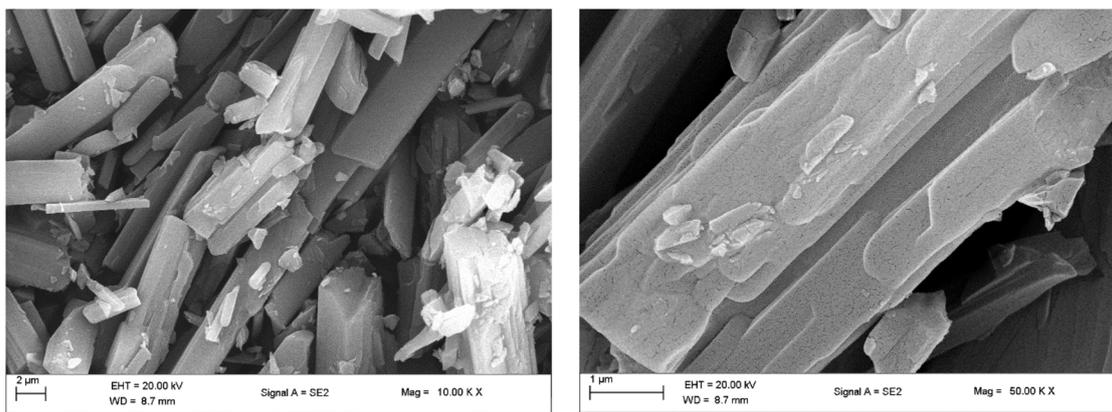
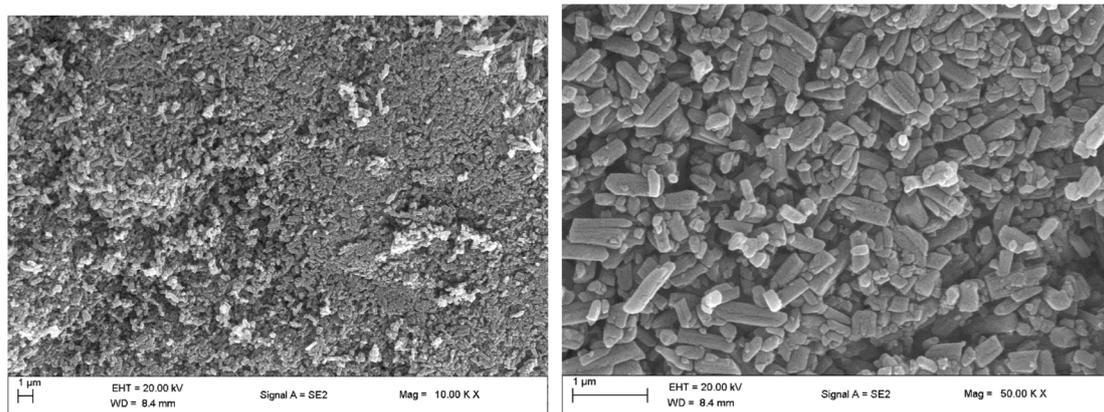**Fig. 14** SEM images of **2** at different magnifications.

Fig. 15 SEM images of **3** at different magnifications.

3.7. Adsorption studies

The adsorption capabilities of MOFs have been extensively studied by numerous researchers. Various factors influence the adsorbability of dissolved substances, including the chemical form of the substance, initial concentration, contact time, temperature, solution pH, and adsorbent dosage. Compounds **1**, **2** and **3** were employed separately for the removal of 2,4-dichlorophenoxyacetic acid through adsorption. The adsorbed quantities of 2,4-dichlorophenoxyacetic acid over compounds **1**, **2** and **3** were monitored by UV-vis at 283 nm (λ_{max}) which was later confirmed by FTIR. The ability of **1**, **2** and **3** to adsorb 2,4-dichlorophenoxyacetic acid from aqueous solutions under different optimized conditions of concentration, time, pH, and temperature were investigated.

3.7.1. Effect of initial concentration. To evaluate the adsorptive performances of compounds **1**, **2**, and **3**, the effects of initial concentrations were examined at a temperature of 30 $\pm$ 2 °C over a period of 3 h, using 0.005 g of MOFs. As shown in Fig. S7, the adsorption of 2,4-dichlorophenoxyacetic acid on compounds **1**, **2**, and **3** increased with increase in concentrations up to 150 mg L^{-1}, after which it began to decrease. The impact of the initial concentration is influenced by the direct

relationship between the herbicide concentration and the available binding sites on the adsorbent surface.[38] The optimal adsorption concentrations were determined to be 486.13 mg g^{-1}, 286.74 mg g^{-1}, and 712.05 mg g^{-1} for compounds **1**, **2**, and **3**, respectively, at a contact time of 3 h. This indicates that at lower herbicide solution concentrations, unoccupied adsorption sites were present, which became occupied as the concentration increased.[4,38,59] At a concentration of 150 mg L^{-1}, once all adsorption sites were saturated with herbicide molecules, desorption of the herbicide molecules began.[4,60] This explains the reduction in the amount of herbicide molecules adsorbed at 200 mg L^{-1} for compounds **1**, **2**, and **3**. The increase in adsorption capacity with rising concentrations of 2,4-dichlorophenoxyacetic acid may be attributed to the higher likelihood of collisions between the adsorbate molecules and the adsorbent surface.[4,61] The high adsorption capacity of 2,4-dichlorophenoxyacetic acid on compound **2** is attributed to its large surface area of 4500 m² g^{-1}. In contrast, the significant adsorption on compound **3** is due to electrostatic interactions between the thiol groups of 1,2-ethanedithiol and the carboxylic acid group of 2,4-dichlorophenoxyacetic acid.

After removal for 3 h, the colour of the Cu-MOFs framework remained unchanged. To confirm the removal of 2,4-

dichlorophenoxyacetic acid over compounds **1**, **2** and **3**, the FT-IR analysis was carried out. The FT-IR spectra of the herbicide adsorbed over of the Cu-MOFs are presented in Fig. S11(a) and (b). The changes observed in the spectra indicated the possible involvement of 2,4-dichlorophenoxyacetic acid functional groups on the surface of the Cu-MOFs after adsorption. It reflects the nature of Cu-MOF and shows significant shift in the bands and intensity changes due to 2,4-dichlorophenoxyacetic acid adsorption.

3.7.2. Effect of contact time. To evaluate the adsorptive performances of compounds **1**, **2**, and **3** including kinetics, the effects of contact time were examined at a temperature of 30 ± 2 °C with the various absorption time (2 min to 180 min), using initial herbicide concentration of 150 mg L^{-1} and 0.005 g of the MOFs. As shown in Fig. S8, the adsorption of 2,4-dichlorophenoxyacetic acid on compounds **1**, **2**, and **3** was rapid at the initial stages of the contact period (2–60 min), and no further increase was observed thereafter. Most of the herbicide removal occurred within the first 60 minutes, with 488.02 mg g^{-1}, 286.74 mg g^{-1} and 720.12 mg g^{-1} of herbicides removed by compounds **1**, **2** and **3**. This may be attributed to the enormous number of available vacant surface sites for adsorption during the initial stages. Over time, the number of vacant sites decreases, due to saturation of the adsorption sites.[4,29,62] Therefore, the time required to reach equilibrium in this study was determined to be 60 minutes.

3.7.3. Effect of pH. The adsorption of herbicide is highly dependent on the pH of the solution. To evaluate the adsorptive performances of compounds **1**, **2**, and **3**, the effects of the solution pH were examined at a temperature of 30 ± 2 °C over a period of 1 h, using 0.005 g of MOFs and 150 mg L^{-1} of the herbicide solution. As shown in Fig. S9, the adsorption of 2,4-dichlorophenoxyacetic acid on compounds **1**, **2**, and **3** increased with increased in pH up to a pH of 4, after which it began to decrease. Similar patterns were observed in the adsorption of 2,4-dichlorophenoxyacetic acid on MIL-53. The reduced adsorption capacity at high pH levels can be attributed to the repulsive electrostatic interactions between the MOFs and the 2,4-D anions, because the pK_a value of 2,4-dichlorophenoxyacetic acid is approximately 2.7–2.8.[29] The optimal adsorption of 472.77 mg g^{-1}, 290.19 mg g^{-1}, and 721.80 mg g^{-1} were obtained for compounds **1**, **2**, and **3**, respectively, at a pH of 4.

3.7.4. Effect of temperature. The adsorption of herbicide also depends on the temperature of the solution. To evaluate the adsorptive performances of compounds **1**, **2**, and **3**, the effects of the solution temperature were examined at a pH of 4 over a period of 1 h, using 0.005 g of MOFs and 150 mg L^{-1} of the herbicide solution. As shown in Fig. S10, the adsorption of 2,4-dichlorophenoxyacetic acid on compounds **1**, **2**, and **3** increased with rising temperature up to 30 °C, after which it begins to decrease. Similar patterns were observed in the adsorption of 2,4-dichlorophenoxyacetic acid on MIL-53.[63] The optimal adsorption of 484.17 mg g^{-1}, 291.90 mg g^{-1}, and 738.48 mg g^{-1} were observed for compounds **1**, **2**, and **3**, respectively, at 30 °C.

3.8. Adsorption isotherms

Adsorption isotherms illustrate the relationship between the quantity of herbicide adsorbed and its concentration at constant temperature. To understand the MOF–2,4-D interaction batch study data were fitted to Langmuir, Freundlich, Temkin and Dubinin–Radushkevich isotherm. These isotherms were obtained after a sufficient adsorption time of 3 h, and the results are compared in Fig. 16 and Table 3.[4,61–66]

For this study, the sorption data have been analyzed using the four isotherm models.[4,61–66] The calculated adsorption capacities (q_m) obtained from the Langmuir fitting experimental data gave a better agreement with those of the experimental values. Also, the correlation coefficients (R^2) of Langmuir model are higher than those of the other isotherm models, therefore Langmuir isotherm is best fit for the three Cu-MOFs. The use of the Langmuir isotherm suggests that surface process plays a significant role in the adsorption of 2,4-dichlorophenoxyacetic acid over **1**, **2** and **3** i.e. adsorption occurs at specific homogeneous sites within the Cu-MOFs and that once 2,4-D occupies a site, no further adsorption can take place at that site.[66] The amount of adsorbed herbicide increases in the order of **2** < **1** < **3** under the experimental conditions, which indicates that a certain quantity of **3** would remove a larger quantity of 2,4-dichlorophenoxyacetic acid compared to **1** and **2**.

3.9. Adsorption kinetic models

To understand the adsorption kinetics of the three Cu(II) MOFs, 2,4-dichlorophenoxyacetic acid was adsorbed at various intervals up to 180 minutes, and the quantity of adsorbed 2,4-
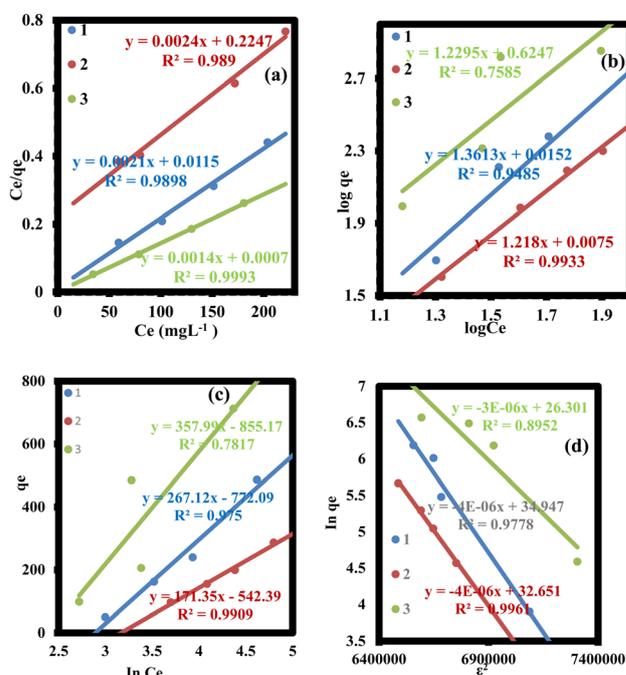

Fig. 16 Adsorption isotherm plot of the 2,4-dichlorophenoxyacetic acid over **1**, **2**, and **3** (a) Langmuir (b) Freundlich (c) Temkin (d) Dubinin–Radushkevich isotherm.

Table 3 Isotherms and rate kinetics parameters and goodness of fit

Isotherms/kinetics	Parameter	Cu-MOF		
		1	**2**	**3**
	q_e, exp. (mg g^{-1})	588.235	333.333	833.333
Langmuir isotherm	q_m (mg g^{-1})	476.190	416.667	714.286
	K_L (L mg^{-1})	0.183	0.011	2.000
	R^2	0.989	0.989	0.999
Freundlich isotherm	K_F (mg g^{-1} (L mg^{-1})$^{1/n}$)	1.036	1.017	4.214
	N	0.735	0.821	0.813
	R^2	0.949	0.993	0.759
Temkin isotherm	b_T	9.275	14.459	6.921
	k_T (L mg^{-1})	0.056	0.042	0.091
	R^2	0.975	0.991	0.782
D–R isotherm	q_s (mg g^{-1})	1.504×10^{15}	1.514×10^{14}	2.645×10^{11}
	E (J mol^{-1})	353.553	353.553	408.248
	R^2	0.978	0.996	0.895
Pseudo 1st order kinetics	K_1 (min^{-1})	0.00525	0.00569	0.00595
	q_e (mg g^{-1})	609.818	349.301	845.084
	R^2	0.979	0.963	0.983
Pseudo 2nd order kinetics	K_2 (g (mg min)$^{-1}$)	5.768×10^{-5}	11.627×10^{-5}	6.000×10^{-5}
	q_e (mg g^{-1})	588.235	333.333	833.333
	R^2	0.980	0.991	0.991

dichlorophenoxyacetic acid is displayed in Fig. S8, with an initial concentration of 150 mg L^{-1}. As illustrated in Fig. S8, the adsorbed quantity of 2,4-dichlorophenoxyacetic acid follows the order of **2** < **1** < **3** throughout the entire adsorption period. The adsorption process for 2,4-dichlorophenoxyacetic acid on **1**, **2**, and **3** is nearly complete within 60 minutes, which suggest rapid adsorption on **1**. Pseudo-first order and pseudo-second order models were used to study the kinetics of the adsorption of 2,4-dichlorophenoxyacetic acid on **1**, **2**, and **3**.[4,66–68]

The plots of the pseudo-first-order kinetics for herbicide adsorption on the three Cu(II)-MOFs at an initial concentration of 150 mg L^{-1} are shown in Fig. 17(a). The adsorption time ranges from 0 to 60 minutes gives good linearity, and the kinetic constants are presented in Table 3. The adsorption kinetic constants for 2,4-dichlorophenoxyacetic acid follow the order **1** < **2** < **3**, indicating that **3** is the most effective adsorbent for 2,4-dichlorophenoxyacetic acid.

Also, for the adsorption of 2,4-dichlorophenoxyacetic acid on **1**, **2**, and **3**, the changes in the adsorbed amount with time are treated with the versatile pseudo-second-order kinetic model, as it effectively handles the entire dataset.[4,63,64] The calculated kinetic constants (k_2) and correlation coefficients (R^2) are presented in Table 3. Like the first-order kinetic constants, the rate constant generally increases in the order of **1** < **2** < **3**, which confirmed more rapid adsorption over **3** compared to the adsorption over **1** and **2**. The rapid adsorption over **3** suggests not only an effect of the pore size but also some specific interactions between the thiol functionality on **3** and the 2,4-dichlorophenoxyacetic acid. However, the linearity of the second order kinetics is relatively better (higher correlation coefficients R^2). For the present study, judging by the R^2 values of the plots in Fig. 17, pseudo-second order kinetic effectively represents the experimental kinetic data for the entire adsorption period with higher R^2 value.
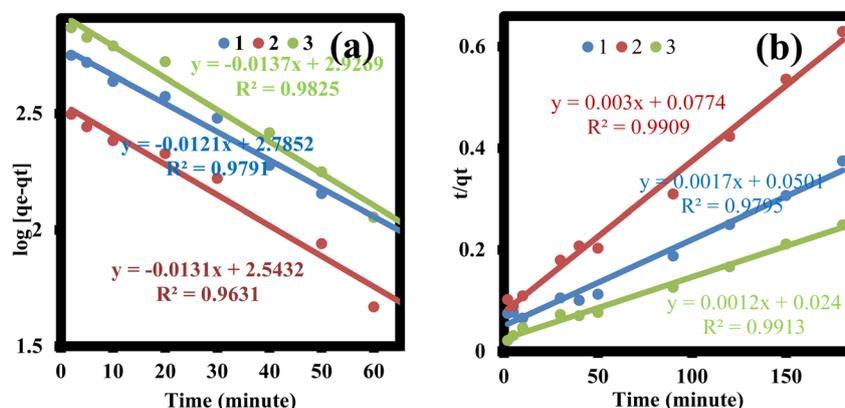

Fig. 17 Plots of the adsorption kinetics of the 2,4-dichlorophenoxyacetic acid adsorption on **1**, **2**, and **3** at 150 mg L^{-1}. (a) Pseudo-first-order kinetics, (b) pseudo-second-order kinetics.

3.10. Characterization of the MOFs after the removal of 2,4-dichlorophenoxyacetic

The FT-IR spectra of the Cu-MOFs (**1**, **2** & **3**), both before and after the removal of 2,4-dichlorophenoxyacetic acid, were compared in the far IR region (4000–600 cm^{-1}) as illustrated in Fig. S11(a) and (b). The adsorption process is confirmed by the emergence of new vibration bands or the enhancement of existing ones, which are characteristic of the 2,4-dichlorophenoxyacetic acid.[69] The band observed at 693 cm^{-1} after adsorption is associated with asymmetric stretches of C–Cl bond in the 2,4-dichlorophenoxyacetic acid molecule.[69,70] The band at 1580 cm^{-1} and 1476 cm^{-1} show the presence of –C═C vibrations of the aromatic ring from the 2,4-dichlorophenoxyacetic acid molecule. Other characteristics band of 2,4-dichlorophenoxyacetic acid molecule such as –C–O bands at 1230 cm^{-1} was observed.[69–72] The spectra show that some peaks were shifted or disappeared and that new peaks were also detected. These changes observed in the spectra indicated the possible involvement of those functional groups on the surface of the Cu-MOFs during the adsorption process.[70]

After the adsorption of 2,4-dichlorophenoxyacetic on **1**, **2** and **3**, all the diffraction peaks were indexed as shown in Fig. S12(a) and (b). The PXRD patterns of **1**, **2** and **3** (before and after), show similar characteristic peaks confirmed that their crystalline property didn't change after the adsorption of 2,4-dichlorophenoxyacetic onto the Cu-MOFs surface.

To investigate the surface area and pore volume of **1**, **2** and **3** before & after the removal of 2,4-dichlorophenoxyacetic, the samples were characterized with Brunauer–Emmett–Teller (BET) analysis as shown in Table 4 and Fig. S13–S18. The isotherms for nitrogen adsorption and desorption at 77 K show a steep slope in their patterns, this indicated that as pressure increases, adsorption increased, and nitrogen tended to occupy the free spaces. As shown in Table 4, the BET surface area of **1**, **2** and **3**, both before and after the removal of 2,4-dichlorophenoxyacetic acid, were compared. After the adsorption of 2,4-dichlorophenoxyacetic acid, it can be observed that the

surface areas decreased, because the herbicide molecules were adsorbed on the surface of the Cu-MOFs.[27] The adsorption isotherm experimental data for compounds **1**, **2** & **3** are shown in Tables T1–T3. True concentration changes of 2,4-dichlorophenoxyacetic in the solution after adsorption has been verified by HPLC to exclude the influence of degradation or volatilization. The removed quantities of 2,4-dichlorophenoxyacetic over **1**, **2** and **3** were monitored by HPLC coupled with a diode array detector (DAD) at 283 nm (λ_{max}) which was later confirmed by FTIR, SEM and BET. From the results obtained from the HPLC analysis, the amount of 2,4-dichlorophenoxyacetic removed was 70%, 50% and 92% over **1**, **2** and **3** respectively.

3.11. Molecular docking

The binding affinity of the selected guest molecule, 2,4-dichlorophenoxyacetic acid (a known herbicide), with the host frameworks (MOF1–3) was investigated using molecular docking. In this study, Induced Fit Docking (IFD) was employed to analyze these interactions.[73,74] The calculated binding energies were negative in all cases, which indicates thermodynamically favourable binding interactions (Table 5).

The adsorptive interactions between the herbicide 2,4-dichlorophenoxyacetic acid (2,4-D) and three metal–organic frameworks (MOF1–3) were investigated *via* Induced Fit Docking (IFD) to evaluate binding affinities and key intermolecular interactions. All three MOFs exhibited negative binding energies, confirming thermodynamically favourable adsorption of 2,4-D.

MOF2 displayed the strongest binding affinity, with a Glide score (*G*-score) of −4.955 kcal mol^{-1} and Glide *E*-model energy of −16.505 kcal mol^{-1}, suggesting superior adsorption capability compared to MOF1 (*G*-score: −4.134 kcal mol^{-1}) and MOF3 (*G*-score: −4.323 kcal mol^{-1}). Furthermore, MOF2 was the only framework to exhibit a conventional hydrogen bond (H⋯O, 1.92 Å), which likely contributes to its enhanced binding affinity. All three MOFs showed non-covalent OH⋯Cu interactions (distances: 3.63–4.85 Å), indicating weak coordinative binding between 2,4-D's hydroxyl group and the MOFs' copper sites. On the other hand, MOF3 had the shortest Cu interaction (3.63 Å), implying slightly stronger metal–herbicide contact despite its moderate *G*-score. The weak OH⋯Cu distances in all three MOFs suggest physisorption rather than chemisorption, which may influence recyclability (Fig. 18).

3.12. DFT calculations

Density functional theory (DFT) calculations were performed on all studied molecules using the Jaguar module in Schrödinger

Table 4 BET surface area & pore volume comparison of **1**, **2** and **3** before & after the removal of 2,4-dichlorophenoxyacetic

		Cu-MOF		
	Parameter	**1**	**2**	**3**
Before	Surface area (m^2 g^{-1})	271.406	236.517	154.752
	Pore volume (cm^3 g^{-1})	0.655	0.989	0.983
After	Surface area (m^2 g^{-1})	62.105	69.401	75.208
	Pore volume (cm^3 g^{-1})	0.998	0.997	0.996

Table 5 Energies, hydrogen bonding and π-interactions of MOF1–3

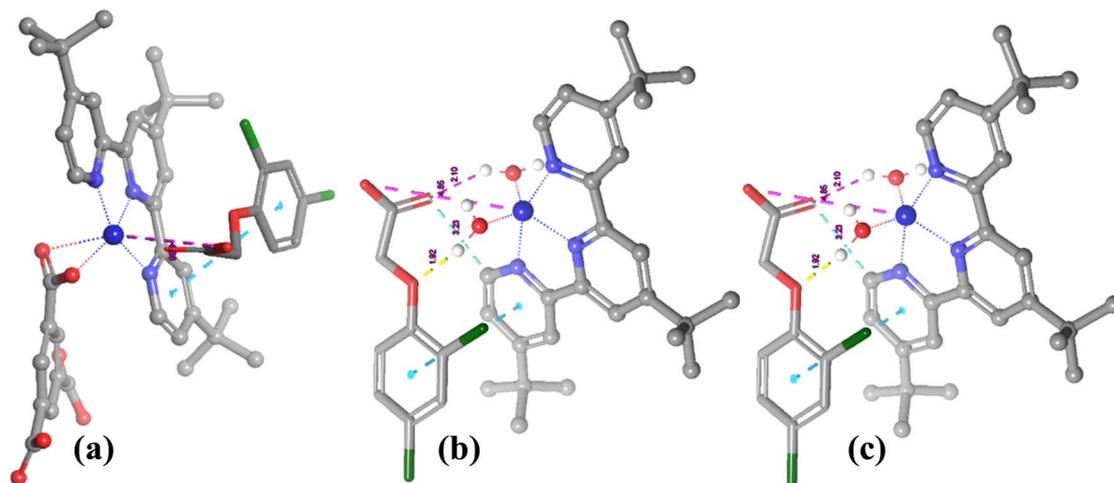| Entry	*G*-Score	Glide *E*-model kcal mol^{-1}	Hydrogen bonds interactions (Å)	π–cation interactions (Å)
1	−4.134	−16.200	—	OH⋯Cu (4.36)
2	−4.955	−16.505	H⋯O (1.92)	OH⋯Cu (4.85)
3	−4.323	−16.401	—	OH⋯Cu (3.63)

Fig. 18 Docked structure of the Cu-MOFs and 2,4-D (a) MOF1 (b) MOF2 and (c) MOF3.

2023-2. Geometry optimizations were carried out at the B3LYP-D3 level of theory, incorporating Becke's three-parameter hybrid exchange functional and the Lee–Yang–Parr (LYP) correlation functional, along with Grimme's D3 dispersion correction. The LANL2DZ basis set was employed for all calculations, with an effective core potential (ECP) for heavy atoms.[75–77]

To simulate physiological conditions, solvation effects were accounted for using the polarizable continuum model (PCM) with water as the solvent.[78] Quantum chemical descriptors, including molecular electrostatic potential (MESP), highest occupied molecular orbital (HOMO), lowest unoccupied molecular orbital (LUMO), and aqueous solvation energy, were computed. Additionally, thermodynamic properties such as zero-point energy (ZPE), enthalpy, Gibbs free energy, and entropy were derived from the DFT calculations.[79]

The combined DFT-derived thermodynamic parameters (ZPE, entropy, enthalpy, free energy) and electronic properties (HOMO, LUMO, E_{gap}, chemical potential, hardness,

electrophilicity) provide a comprehensive understanding of the adsorption behaviour of 2,4-D on MOF1–3 (Fig. 19) (Tables 6 and 7).

The HOMO of 2,4-D is primarily localized on the chlorido substituent at the *para* position, an indication of its role as an electron-donating group, while the LUMO is concentrated on the benzene ring, which indicates an electrophilic character. This distribution implies that 2,4-D can participate in charge-transfer interactions. In MOF1, the α-HOMO is localized on a DMF solvent molecule, while the α-LUMO resides on the ter-pyridine moiety. The β-HOMO also lies on DMF, whereas the β-LUMO is distributed across the central copper(II) ion that is coordinated to the nitrogen, and a hydroxyl group of the benzenetricarboxylate (btc) linker. This orbital arrangement suggests that DMF may compete with 2,4-D for binding at the copper site, potentially hindering herbicide adsorption. The presence of solvent-occupied HOMOs implies that activation (DMF removal) could enhance 2,4-D uptake by freeing up metal
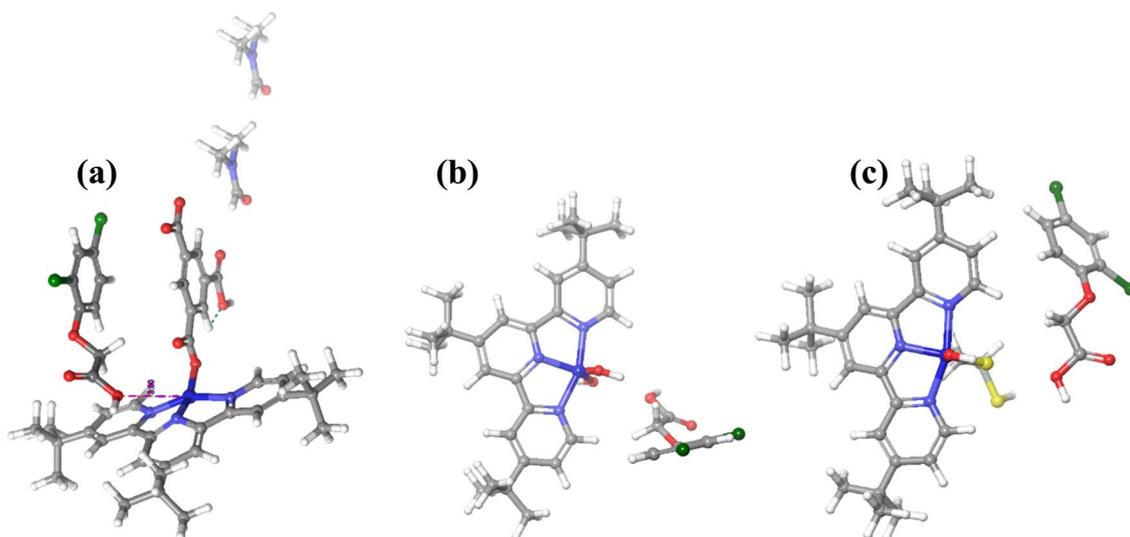

Fig. 19 The optimized geometrical structure of 2,4-dichlorophenoxyacetic acid adsorbed onto the three Cu-MOFs (a) MOF1 (b) MOF2 and (c) MOF3.

Table 6 Global reactivity indicators of studied molecules

Entry	HOMO	LUMO	E_{gap}	μ	χ	H	S	ω
2,4D	−6.82	−0.98	5.84	−3.90	3.90	2.92	0.17	2.60
MOF1	−5.87	−3.14	2,73	−4.51	4.51	1.37	0.37	7.44
MOF2	−7.59	−6.38	**1.22**	−6.99	6.99	0.61	0.82	40.07
MOF3	−7.12	−6.50	**0.62**	−6.81	6.81	0.31	1.61	74.56
MOF1@herbicide	−6.14	−3.18	2.96	−4.66	4.66	1.48	0.34	7.33
MOF2@herbicide	−8.34	−5.01	3.32	−6.68	6.68	1.66	0.30	13.42
MOF3@herbicide	−6.92	−5.42	**1.50**	−6.17	6.17	0.75	0.67	25.43

Table 7 Thermodynamic properties

Entry	ZPE	Entropy	Enthalpy	Free energy
Herbicide and free MOFs				
2,4-D	81.012	97.072	6.349	−22.593
MOF1	566.599	217.854	24.394	−40.559
MOF2	372.969	171.138	17.588	−33.437
MOF3	421.033	175.812	18.045	−34.373
MOF/herbicide complex				
MOF1@2,4-D	648.574	253.333	30.003	−45.529
MOF2@2,4-D	68.900	95.364	4.143	−24.290
MOF3@2,4-D	491.141	212.039	23.720	−39.500

ion sites for interaction with the herbicide's electron-donating chlorido group (Fig. S22–S24 and S31–S33).

The α-HOMO for MOF2 is located on a methyl group of the terpyridine ligand, while the α-LUMO is distributed over the terpyridine nitrogen, copper(II) centre, and bound hydroxyl groups. The β-HOMO mirrors the α-HOMO, whereas the β-LUMO is centred on the copper(II) ions and its immediate coordination sphere (including water ligands). Upon 2,4-D adsorption, the α-HOMO of the MOF2@2,4-D complex shifts to the copper(II) centre, hydroxyl groups, and the carbonyl/oxygen groups of 2,4-D, while the α-LUMO remains on the copper-terpyridine-hydroxyl network. The β-HOMO extends to the 2,4-D benzene ring and chlorido substituents, and the β-LUMO localizes on the herbicide, indicating significant back-donation from the MOF to 2,4-D. These interactions suggest a cooperative binding mechanism, where Cu(II) acts as a Lewis acid site, while the terpyridine and hydroxyl groups stabilize the herbicide *via* π-stacking and hydrogen bonding. However, the rigid terpyridine framework may limit pore accessibility, responsible for MOF2's lower experimental adsorption capacity compared to MOF3 (Fig. S25–S27 and S36–S38).

In MOF3, the functionalization with 1,2-ethanedithiol (TH) drastically alters the electronic structure. Both α- and β-HOMOs are localized on the thiol groups, while the α-LUMO remains on the thiol and the β-LUMO on the copper-nitrogen core. This suggests that the thiol groups serve as strong electron donors, and enhances the interactions with 2,4-D's LUMO (benzene ring). In the MOF3@2,4-D complex, the α-HOMO shifts to the *para*-chlorido group of 2,4-D, while the α-LUMO moves to the Cu–N/O core, indicating thiol-to-herbicide charge transfer. The β-HOMO remains on the chlorido group, and the β-LUMO on the copper(II) centre, that reinforces a Cu-thiol-2,4-D electron

relay. This mechanism aligns with MOF3's superior adsorption capacity (833.33 mg g^{-1}), as the soft thiol groups form covalent-like interactions with the herbicide, that surpasses the weaker electrostatic/coordination binding in MOF1 and MOF2 (Fig. S28–S30 and S39–S41).

Frontier orbital and thermodynamic analyses reveal that MOF3's unmatched 2,4-D adsorption (833.33 mg g^{-1}) arises from thiol-mediated charge transfer (ΔE = 0.62 eV), where electron delocalization from 1,2-ethanedithiol (HOMO = −7.12 eV) to the herbicide's LUMO (−0.98 eV) creates a covalent-like interaction (ω = 74.56 eV). This soft–soft binding is entropically stabilized (ΔS = 212.039 cal mol^{-1} K^{-1}) and overcome the endothermic penalty (ΔH = 23.720 kcal mol^{-1}). In contrast, MOF2's rigid terpyridine framework (η = 1.66 eV) restricts reorganization, that leads to a less favourable ΔG (−24.290 kcal mol^{-1}) despite strong initial H-bonding (IFD). MOF1's anomalous ΔG (−45.529 kcal mol^{-1}) reflects DMF solvation effects, that emphasizes the need for solvent-free activation.

3.13. Reusability of 1, 2 and 3

To evaluate the recyclability of compounds **1**, **2** and **3**, we performed six adsorption loop experiments to assess their reusability. Following the herbicide removal process, the residual powder was soaked in 10 mL of ethanol for 48 h, with the ethanol being replaced three times. After the adsorption process, the residue powder was immersed in 20 mL of water for 72 h, and exchanged the water five times. After that, the sample was dried under vacuum at 100 °C for 24 h. Furthermore, the FT-IR of compounds **1**, **2** and **3**, both before and after removal of 2,4-di-chlorophenoxyacetic acid exhibited no substantial alterations in structural stability (as shown in Fig. S11 and S19). Similarly to the FT-IR, the PXRD of compounds **1**, **2** and **3**, before and after adsorption of 2,4-dichlorophenoxyacetic acid have similar diffraction patterns and this confirms the framework stability of the Cu-MOFs after recycling (as shown in Fig. S12 and S46). Nevertheless, the adsorption capacity of compounds **1**, **2**, and **3** showed a slight decrease with each cycle, potentially due to physicochemical adsorption or the loss of adsorbent during the cycling process. These findings are consistent with previous studies.[80–84]

3.14. Conclusions

Copper(II) metal organic frameworks of 4,4′,4″-tri-*tert*-butyl-2,2′:6′,2″-terpyridine was synthesized and characterized by elemental analyses, FT-IR spectroscopy and mass

spectrometry. The molecular structure of compound **1** reveals the Cu(II) ion is in a five-coordinate geometry. Compound **1**, $[Cu(btc)(N3ttb)]_2 \cdot (DMF)_2$, contained two coordinated benzene 1,3,5-tricarboxylic acid (BTA), and the two coordinated terpyridine molecules (TPD) to the copper(II) ions. The compound crystallized with two molecules of dimethylformamide (DMF) acting as solvent of crystallization. Compound **2** was functionalized with a thiol group to form compound **3** and characterized by elemental analyses, FTIR, PXRD and SEM. The data obtained from the adsorption process indicate that the functionalized MOFs **3** have a higher adsorption capacity than **1** & **2** which could be ascribed to electrostatic interactions between the thiol groups of 1,2-ethanedithiol and the carboxylic acid group of 2,4-dichlorophenoxyacetic acid. The kinetics study results showed that the adsorption of 2,4-dichlorophenoxyacetic acid over $[Cu(btc)(N_3ttb)] \cdot (DMF)_2$ **1**, $[Cu(N_3ttb)(H_2O)_2]$ **2** and $[Cu(N_3ttb)(H_2O)_2]$–TH **3** followed the pseudo-second-order rate law and the Langmuir isotherm was found to be the most suitable to describe the adsorption process. Global reactivity indices elucidate why MOF3 outperforms MOF1 and MOF2 in herbicide adsorption. MOF3's ultra-soft character ($\eta = 0.31$ eV, $S = 1.61$ eV^{-1}) and high electrophilicity ($\omega = 74.56$ eV) enable charge-transfer-driven binding, yielding both favourable ΔG (-39.500 kcal mol^{-1}) and high experimental capacity (833.33 mg g^{-1}). In contrast, MOF2's hardness ($\eta = 0.61$ eV) and rigidity lead to entropic penalties ($\Delta S = 95.364$ cal mol^{-1} K^{-1}), despite its strong initial docking (IFD). MOF1's intermediate properties reflect solvent-mediated effects, underscoring the need to activate pores for practical applications. Thus, it is proposed that MOFs hold great potential as adsorbents for the removal of 2,4-dichlorophenoxyacetic acid from wastewater.

Author contributions

Sunday J. Olatunji: investigation, data curation, formal analysis, writing original draft and visualization. Adedibu C. Tella: project administration, supervision, conceptualization, methodology, writing review and editing. Solomon O. Oloyede: data curation, formal analysis, writing original draft and visualization. Peter A. Ajibade: conceptualization, project administration, supervision, funding acquisition, methodology, writing review and editing. Allen T. Gordon: investigation, data curation and visualization. Adeniyi S. Ogunlaja: visualization, writing review and editing.

Conflicts of interest

There are no conflicts to declare.

Data availability

CCDC 2209311 contains the supplementary crystallographic data for this paper.[85]

All other data for the finding presented in this study are within the supplementary information (SI). Supplementary information is available. See DOI: https://doi.org/10.1039/d5ra07218b.

Acknowledgements

References

1 H. Mondol and S. H. Jhung, *Chem. Eng. J.*, 2021, **421**, 129688.

2 J. Liu and W. Yang, *Science*, 2012, **337**, 649–650.

3 A. Rolston, *Nature*, 2016, **536**, 396.

4 A. C. Tella, S. O. Owalude, S. J. Olatunji, V. O. Adimula, S. E. Elaigwu, L. O. Alimi, P. A. Ajibade and O. S. Oluwafemi, *J. Environ. Sci.*, 2018, **64**, 264–275.

5 M. D. Olawale, A. C. Tella, J. A. Obaleye and J. S. Olatunji, *New J. Chem.*, 2020, **44**, 3961–3969.

6 S. Lal, P. Singh, A. Singhal, S. Kumar, A. P. S. Gahlot, N. Gandhi and P. Kumari, *RSC Adv.*, 2024, **14**, 3413–3446.

7 D. X. Flores-Cervantes, C. Medina-Montiel, N. Ramirez-Corona and R. Navarro-Amador, *Air, Soil Water Res.*, 2022, **15**, DOI: 10.1177/11786221221080183.

8 A. Yohannes, Y. Su and S. Yao, *ACS Symp. Ser.*, 2021, 1–23.

9 A. J. Howarth, Y. Liu, J. T. Hupp and O. K. Farha, *CrystEngComm*, 2015, **17**, 7245–7253.

10 M.-A. Gatou, I.-A. Vagena, N. Lagopati, N. Pippa, M. Gazouli and E. A. Pavlatou, *Nanomaterials*, 2023, **13**, 2224.

11 S. Deng, Y. Chen, D. Wang, T. Shi, X. Wu, X. Ma, X. Li, R. Hua, X. Tang and Q. X. Li, *J. Hazard. Mater.*, 2015, **297**, 17–24.

12 M. A. Matouq, Z. A. Al-Anber, T. Tagawa, S. Aljbour and M. Al-Shannag, *Ultrason. Sonochem.*, 2008, **15**, 869–874.

13 P. A. Diaw, N. Oturan, M. D. G. Seye, A. Coly, A. Tine, J. J. Aaron and M. A. Oturan, *Sep. Purif. Technol.*, 2017, **186**, 197–206.

14 H. Rubí-Juárez, S. Cotillas, C. Sáez, P. Cañizares, C. Barrera-Díaz and M. A. Rodrigo, *Appl. Catal., B*, 2016, **188**, 305–312.

15 G. R. Boyd, H. Reemtsma, D. A. Grimm and S. Mitra, *Sci. Total Environ.*, 2003, **311**, 135–149.

16 G. R. Boyd, S. Zhang and D. A. Grimm, *Water Res.*, 2005, **39**, 668–676.

17 C. Rice, *Removal of hormones and antibiotics by nanofiltration membranes*, https://www.academia.edu/78602984/Removal_of_hormones_and_antibiotics_by_nanofiltration_membranes, accessed 27 August 2024.

18 T. A. Ternes, J. Stüber, N. Herrmann, D. McDowell, A. Ried, M. Kampmann and B. Teiser, *Water Res.*, 2003, **37**, 1976–1982.

19 T. Islamoglu, Z. Chen, M. C. Wasson, C. T. Buru, K. O. Kirlikovali, U. Afrin, M. R. Mian and O. K. Farha, *Chem. Rev.*, 2020, **120**, 8130–8160.

20 A. Dąbrowski, P. Podkościelny, Z. Hubicki and M. Barczak, *Chemosphere*, 2005, **58**, 1049–1070.

21 M. Brigante and M. Avena, *Microporous Mesoporous Mater.*, 2014, **191**, 1–9.

22 Z. Zhou and M. Hartmann, *Chem. Soc. Rev.*, 2013, **42**, 3894.

23 M. R. Benzigar, S. N. Talapaneni, S. Joseph, K. Ramadass, G. Singh, J. Scaranto, U. Ravon, K. Al-Bahily and A. Vinu, *Chem. Soc. Rev.*, 2018, **47**, 2680–2721.

24 Y. Zu, S. Wang, Y. Hui, N. Ni, X. Zhang, Y. Qin, L. Zhang, H. Liu, X. Gao and L. Song, *Chem. Eng. J.*, 2020, **401**, 126112.

25 H. Duan, X. Hu and Z. Sun, *J. Hazard. Mater.*, 2020, **384**, 121406.

26 J. A. S. Costa, R. A. de Jesus, D. O. Santos, J. F. Mano, L. P. C. Romão and C. M. Paranhos, *Microporous Mesoporous Mater.*, 2020, **291**, 109698.

27 A. C. Tella, S. J. Olatunji and P. A. Ajibade, *RSC Adv.*, 2024, **14**, 25759–25770.

28 M. Sarker, S. Shin and S. H. Jhung, *ACS Omega*, 2019, **4**, 9860–9867.

29 Z. Hasan, E.-J. Choi and S. H. Jhung, *Chem. Eng. J.*, 2013, **219**, 537–544.

30 F. Ke, L.-G. Qiu, Y.-P. Yuan, F.-M. Peng, X. Jiang, A.-J. Xie, Y.-H. Shen and J.-F. Zhu, *J. Hazard. Mater.*, 2011, **196**, 36–43.

31 Z. Q. Yin, S. Wan, J. Yang, M. Kurmoo and M.-H. Zeng, *Coord. Chem. Rev.*, 2017, **378**, 500–512.

32 S. Mukherjee, S. Dutta, Y. D. More, S. Fajal and S. K. Ghosh, *Dalton Trans.*, 2021, **50**, 17832–17850.

33 Y. Qin, M. Hao, D. Wang and Z. Li, *Dalton Trans.*, 2021, **50**, 13201–13215.

34 O. V. Dolomanov, L. J. Bourhis, R. J. Gildea, J. A. K. Howard and H. Puschmann, *J. Appl. Crystallogr.*, 2009, **42**, 339–341.

35 G. M. Sheldrick, *Acta Crystallogr.*, 2015, **71**, 3–8.

36 G. M. Sheldrick, *Acta Crystallogr.*, 2008, **64**, 112–122.

37 S. Bajpai, N. Chand and M. Mahendra, *Water SA*, 2014, **40**, 49–56.

38 S. E. Elaigwu, V. Rocher, G. Kyriakou and G. M. Greenway, *J. Ind. Eng. Chem.*, 2014, **20**, 3467–3473.

39 A. C. Tella, J. A. Obaleye, M. D. Olawale, J. M. Vianney Ngororabanga, A. S. Ogunlaja and S. A. Bourne, *C. R. Chim.*, 2019, **22**, 3–12.

40 A. C. Tella, N. J. Shamle, J. A. Obaleye, A. C. Whitwood, S. A. Bourne and P. A. Ajibade, *J. Mol. Struct.*, 2020, **1209**, 127925.

41 Y. G. Chung, E. Haldoupis, B. J. Bucior, M. Haranczyk, S. Lee, H. Zhang, K. D. Vogiatzis, M. Milisavljevic, S. Ling, J. S. Camp, B. Slater, J. I. Siepmann, D. S. Sholl and R. Q. Snurr, *J. Chem. Eng. Data*, 2019, **64**, 5985–5998.

42 A. K. Patel, R. N. Jadeja and R. J. Butcher, *J. Indian Chem. Soc.*, 2021, **98**, 100182.

43 D. Kovala-Demertzi, M. Staninska, I. Garcia-Santos, A. Castineiras and M. A. Demertzis, *J. Inorg. Biochem.*, 2011, **105**, 1187–1195.

44 E. Macedi, P. Rossi, M. Formica, L. Giorgi, M. Lippi, R. Montis, D. Paderni, P. Paol and V. Fusi, *J. Mol. Struct.*, 2024, **1299**, 137146.

45 A. Neacsu, V. Chihaia, V. Alexiev, G. B. Hadjichristov and S. Minkovska, *Materials*, 2025, **18**, 2505.

46 G. Bolla, B. Sarma and A. K. Nangia, *Chem. Rev.*, 2022, **122**, 11514–11603.

47 S. F. Kainat, M. Hawsawi, E. U. Mughal, N. Naeem, A. M. Almohyawi, H. M. Altass, E. M. Hussei, A. Sadiq, Z. Moussa, A. S. Abd-El-Aziz and S. A. Ahmed, *RSC Adv.*, 2024, **14**, 21464–21537.

48 T. V. N. Thi, C. L. Luu, T. C. Hoang, T. Nguyen, T. H. Bui, P. H. Duy Nguyen and T. P. P. Thi, *Adv. Nat. Sci.:Nanosci. Nanotechnol.*, 2013, **4**, 035016.

49 A. Şengül and O. Büyükgüngör, *Acta Crystallogr., Sect. C:Cryst. Struct. Commun.*, 2005, **61**, 119–121.

50 A. H. Bakheit, H. A. Abuelizz and R. Al-Salahi, *Crystals*, 2023, **13**, 1410.

51 K. Kumara, M. Jyothi, S. Kouser, A. H. U. Kumar, I. Warad, S. A. Khanum and N. K. Lokanath, *J. Mol. Struct.*, 2023, **1272**, 134226.

52 M. A. Spackman and P. G. Byrom, *Chem. Phys. Lett.*, 1997, **267**, 215–220.

53 P. R. Spackman, M. J. Turner, J. J. McKinnon, S. K. Wolff, D. J. Grimwood, D. Jayatilaka and M. A. Spackman, *J. Appl. Crystallogr.*, 2021, **54**, 1006–1011.

54 R. Kumar, T. Guchhait, V. Subramaniyan and G. Mani, *J. Mol. Struct.*, 2019, **1195**, 1–9.

55 M. A. Spackman and D. Jayatilaka, *CrystEngComm*, 2009, **11**, 19–32.

56 *Organic Spectroscopy: Principles And Applications, 2/E by J. Mohan: New N.A. (2018) | Books in my Basket*, https://www.abebooks.com/servlet/BookDetailsPL?bi=30606439474&cm_sp=rec-pd_hw_o_1-_-bdp&reftag=pd_hwo1, accessed 12 January 2023.

57 S. Jain, T. A. Khan, Y. P. Patil, D. Pagariya, N. Kishore, S. Tapryal, A. D. Naik and S. G. Naik, *J. Photochem. Photobiol., B*, 2017, **174**, 35–43.

58 A. Harchani and A. Haddad, *Theor. Chem. Acc.*, 2018, **137**, 90.

59 N. Kannan and M. M. Sundaram, *Dyes Pigm.*, 2001, **51**, 25–40.

60 H. A. Al-Aoh, M. J. Maah, R. Yahya and R. Bin, *Asian J. Chem.*, 2013, **25**, 9573–9581.

61 A. H. Al-Muhtaseb, K. A. Ibrahim, A. B. Albadarin, O. Ali-khashman, G. M. Walker and M. N. M. Ahmad, *Chem. Eng. J.*, 2011, **168**, 691–699.

62 E. M. Cuerda-Correa, J. R. Domínguez, F. J. Olivares-Marín and B. de Heredia, *J. Hazard. Mater.*, 2010, **177**, 1046–1053.

63 B. K. Jung, Z. Hasan and S. H. Jhung, *Chem. Eng. J.*, 2013, **234**, 99–105.

64 Y. S. Ho and G. McKay, *Process Biochem*, 1999, **34**, 451–465.

65 S. M. Hasany, M. M. Saeed and M. Ahmed, *J. Radioanal. Nucl. Chem.*, 2002, **252**, 477–484.

66 M. A. Rauf, S. B. Bukallah, F. A. Hamour and A. S. Nasir, *Chem. Eng. J.*, 2008, **137**, 238–243.

67 N. A. Khan, Z. Hasan and S. H. Jhung, *J. Hazard. Mater.*, 2013, **244–245**, 444–456.

68 S. Manna, P. Saha, D. Roy, R. Sen and B. Adhikari, *J. Taiwan Inst. Chem. Eng.*, 2016, **67**, 292–299.

69 V. Lima, P. Ivo, W. Evaristo, M. Dias, J. E. Oliveira and J. M. Marconcini, *SN Appl. Sci.*, 2019, **1**, 1212.

70 P. Bartczak, S. Żółtowska, M. Norman, Ł. Klapiszewski, J. Zdarta, A. Komosa, I. Kitowski, F. Ciesielczyk and T. Jesionowski, *Adsorpt. Sci. Technol.*, 2015, **22**, 517–529.

71 N. S. Trivedi, R. A. Kharkar and S. A. Mandavgane, *Arabian J. Chem.*, 2019, **12**, 4541–4549.

72 J. I. Pérez-Martínez, J. M. Ginés, E. Morillo, M. L. G. Rodríguez and J. R. Moyano, *Environ. Technol.*, 2000, **21**, 209–216.

73 A. J. Clark, P. Tiwary, K. Borrelli, S. Feng, E. B. Miller, R. Abel, R. A. Friesner and B. J. Berne, *J. Chem. Theory Comput.*, 2016, **12**, 2990–2998.

74 T. Xu, K. Zhu, A. Beautrait, J. Vendome, K. W. Borrelli, R. Abel, R. A. Friesner and E. B. Miller, *J. Chem. Theory Comput.*, 2022, **18**, 5710–5724.

75 A. T. Gordon, E. C. Hosten and A. S. Ogunlaja, *Pharmaceuticals*, 2022, **15**, 1240.

76 X. Xu and D. G. Truhlar, *J. Chem. Theory Comput.*, 2011, **8**, 80–90.

77 Y. Yang, M. N. Weaver and K. M. Merz, *J. Phys. Chem. A*, 2009, **113**, 9843–9851.

78 E. E. Romero and F. E. Hernandez, *Phys. Chem. Chem. Phys.*, 2018, **20**, 1198–1209.

79 J. John Marshal, B. B. Kuriakose, A. H. Alhazmi and K. Muthusamy, *J. Cell. Biochem.*, 2023, **124**, 434–445.

80 X. Liu, Y. Wang, J. Yuan, X. Li, S. Wu, Y. Bao, Z. Feng, F. Ou and Y. He, *Bioengineering*, 2022, **9**, 517.

81 M. Vesali-Naseh, M. R. V. Naseh and P. Ameri, *J. Cleaner Prod.*, 2021, **291**, 125917.

82 Y. Zheng, F. Rao, M. Zhang, J. Li and W. Huang, *Clean. Eng. Technol.*, 2021, **5**, 100344.

83 M. A. Ghasemzadeh, M. H. Abdollahi-Basir and B. Mirhosseini-Eshkevari, *Green Chem. Lett. Rev.*, 2018, **11**, 47–53.

84 A. C. Oladipo, A. D. Aderibigbe, V. T. Olayemi, P. A. Ajibade, H. S. Clayton, G. J. Clarkson, R. I. Walton and A. C. Tella, *J. Photochem. Photobiol., A*, 2024, **448**, 115331.

85 CCDC 2209311: Experimental Crystal Structure Determination, 2025, DOI: 10.5517/ccdc.csd.cc2d4z3n.